AIMS Mathematics, 11(11): 36593–36633.
DOI: 10.3934/math.20261415
Received: 10 September 2026
Revised: 26 October 2026
Accepted: 28 October 2026
Published: 05 November 2026

http://www.aimspress.com/journal/Math

Research article

A new generalization of Hjorth distribution: Theoretical properties, classical and Bayesian estimation, and applications

Mazen Nassar*

Department of Statistics, Faculty of Science, King Abdulaziz University, Jeddah 21589, Saudi Arabia

* **Correspondence:** Email: mmohamad3@kau.edu.sa; mezo10011@gmail.com.

Abstract: Accurately modeling complex lifetime data remains a central challenge in reliability and survival analysis, particularly when traditional models fail to capture diverse distributional behaviors. In this study, a novel and flexible distribution, referred to as the generalized Hjorth model, is introduced to address these limitations. Graphical illustrations demonstrate that the proposed model can exhibit different probability density function shapes under selected parameter configurations, while its hazard rate function accommodates a wide range of behaviors. A comprehensive theoretical investigation is conducted, including the derivation of key statistical properties and reliability measures. In particular, the shape characteristics of the hazard rate function are examined, demonstrating the ability of the model to represent increasing, decreasing, and non-monotonic hazard structures. Parameter estimation is performed using both maximum likelihood and Bayesian approaches, where the latter is implemented through Markov chain Monte Carlo techniques under the squared error loss function. The performance of the estimators is evaluated through a simulation study, showing generally improved estimation accuracy as the sample size increases under the parameter settings considered. The practical usefulness of the proposed model is further illustrated through the analysis of two real datasets. For the aircraft windshield data, the proposed model provides the closest empirical fit according to the goodness-of-fit measures, although the Hjorth model is favored by the information criteria. For the patient lifetime data, the proposed model is favored by the information criteria and provides the closest empirical fit among the considered models. Comparisons with its submodels and two competing models further demonstrate its modeling flexibility, although the extent of improvement depends on the characteristics of the data. Overall, the findings support the generalized Hjorth model as a flexible alternative for modeling lifetime data.

Keywords: Hjorth distribution; bathtub shape; reliability function; order statistics; Bayesian estimation
Mathematics Subject Classification: 62F10, 62F15, 62N01, 62N05

1. Introduction

Probability distributions constitute the fundamental building blocks of statistical modeling and inference, providing essential tools for describing uncertainty and variability in real-world phenomena. Over the past decades, continuous probability models have played a central role in a wide range of scientific and applied disciplines, including engineering, economics, finance, actuarial science, medicine, and life sciences. In particular, the analysis of lifetime and reliability data relies heavily on the availability of flexible distributions capable of accurately representing diverse failure mechanisms and complex stochastic behaviors. One of the most effective and widely adopted strategies for enhancing models' flexibility is the introduction of additional shape parameters into the existing baseline distributions. This approach allows for greater control over the behavior of both the probability density function (PDF) and the associated hazard rate function (HRF), thereby improving the model's ability to accommodate a wide spectrum of data patterns. In particular, the inclusion of extra parameters can significantly improve the ability to capture tail behavior, skewness, and various hazard rate shapes such as increasing, decreasing, bathtub, or unimodal forms. For instance, Azzalini [1] introduced the skew-normal model to incorporate asymmetry, while Mudholkar and Srivastava [2] proposed the exponentiated Weibull distribution to allow for more flexible hazard rate shapes. Moreover, Marshall and Olkin [3] developed a general parameter augmentation framework that generates flexible classes of distributions, especially for exponential and Weibull baselines. In a related direction, Mahdavi and Kundu [4] introduced an extension mechanism based on adding an additional shape parameter to a baseline model.

A considerable body of literature has further explored methodologies for extending classical distributions, including transformation techniques, compounding schemes, and generator-based families. For example, Eugene et al. [5] proposed the beta-generated family, while Alzaatreh et al. [6] introduced the T-X family as a unified framework for constructing new distributions. Comprehensive reviews of these developments were provided by Lee et al. [7] and Jones [8], whereas Abdelaziz et al. [9] presented a detailed study of Weibull-based generalized families and their applications in lifetime data analysis. Despite the wide variety of classical distributions available in the literature, practical applications frequently reveal limitations in their ability to adequately capture key features of empirical data. Real datasets, especially in reliability and survival analysis, often exhibit pronounced skewness, heavy tails, non-monotonic HRFs, and varying degrees of kurtosis. Such characteristics cannot always be satisfactorily modeled using standard distributions with fixed structural forms. Consequently, there has been a sustained and growing interest in developing more adaptable and flexible distributional frameworks.

One of the most flexible distributions, yet not extensively studied in the literature, is the Hjorth (Hj) distribution introduced by Hjorth [10]. This model is particularly attractive due to its ability to accommodate a variety of hazard rate shapes, including constant, increasing, decreasing, and bathtub forms, while involving only two parameters. Such flexibility makes it a competitive alternative to several classical lifetime distributions. From a structural viewpoint, the Hj distribution admits an insightful interpretation. Its survival function can be expressed as the product of the survival functions of the Rayleigh and Lomax distributions. Consequently, it can be naturally interpreted within a competing risk framework, which enhances its applicability in modeling complex failure mechanisms; see Hjorth [10]. Further insights into the Hj model were provided by Guess and Nam [11], who

investigated the behavior of its mean residual life function. The ability of the model to capture a wide range of hazard rate shapes makes it particularly suitable for analyzing lifetime data, thereby highlighting its practical relevance in reliability and survival analysis.

Let X be a random variable following the Hj distribution with parameter vector $\boldsymbol{\theta} = (\lambda, \alpha)^\top$, where $\lambda > 0$ is a rate parameter and $\alpha > 0$ is a shape parameter. The main distributional functions are given as follows. The PDF is

$$f(x;\boldsymbol{\theta}) = \frac{\alpha + \lambda x(1+x)}{(1+x)^{\alpha+1}} \exp\left(-\tfrac{1}{2}\lambda x^2\right), \quad x > 0, \tag{1.1}$$

the cumulative distribution function (CDF) is

$$F(x;\boldsymbol{\theta}) = 1 - \frac{\exp\left(-\tfrac{1}{2}\lambda x^2\right)}{(1+x)^{\alpha}}, \tag{1.2}$$

the reliability (survival) function (RF) is

$$R(x;\boldsymbol{\theta}) = \frac{\exp\left(-\tfrac{1}{2}\lambda x^2\right)}{(1+x)^{\alpha}}, \tag{1.3}$$

and the HRF is given by

$$h(x;\boldsymbol{\theta}) = \lambda x + \frac{\alpha}{1+x}. \tag{1.4}$$

Despite these appealing properties, the inferential aspects of the Hj distribution, particularly under complex sampling and censoring schemes, have not been thoroughly explored. Existing contributions, including those by Yadav et al. [12], Pushkarna et al. [13], Elshahhat and Nassar [14], and Alotaibi et al. [15], remain relatively limited.

Further extensions of the Hj model are of practical interest for increasing the flexibility of its PDF and HRF while retaining a relatively small number of parameters. Although numerous lifetime models have been developed using additive hazards and competing risks constructions, several related models require four or more parameters. Examples include the four-parameter additive Weibull model of Xie and Lai [16], the six-parameter additive Burr XII model of Wang [17], the four-parameter additive Perks–Weibull model of Singh [18], the four-parameter additive Chen model of Méndez-González et al. [19], and the four-parameter flexible exponential power–Weibull model of Ghazal [20]. These developments motivate the introduction of a flexible extension of the Hj model with fewer parameters.

The present study introduces the generalized Hj (GHj) distribution through a competing risks framework involving independent Lomax and Weibull lifetimes. Its RF is the product of the component RFs, providing a direct interpretation of the underlying risks. The resulting distribution has only three parameters: One rate parameter and two shape parameters. The Weibull component contributes additional flexibility through its shape parameter; see Hallinan [21] and Pham and Lai [22] for discussions of the Weibull model. Specifically, the extension introduces a free Weibull shape parameter β into the Hj structure, which is recovered when $\beta = 2$ under the corresponding rate reparameterization.

Although the competing risks construction itself is established, allowing β to vary broadens the attainable hazard behavior to include strictly decreasing, strictly increasing, bathtub-shaped, and

increase–decrease–increase HRFs. A constant HRF is also recovered in the limiting exponential case when $\beta = 1$ and $\alpha \to 0^+$. The combination of this hazard flexibility and a three-parameter formulation provides a relatively parsimonious alternative to the related models discussed above. The GHj model also differs structurally from the Weibull–Lomax (WL) distribution proposed by Tahir et al. [23], whose RF is obtained through a transformation of the Lomax distribution rather than the product of Lomax and Weibull RFs. The practical value of the additional parameter is assessed through direct comparisons with the Hj, Weibull, Lomax, and Weibull–Lomax (WL) models, as well as the flexible Weibull extension (FWE) model proposed by Bebbington et al. [24], considering both goodness of fit and the model complexity. In the first application, the Hj model has lower information criteria, whereas the GHj model yields smaller goodness-of-fit statistics. In the second application, the GHj model has the lowest information criteria and goodness-of-fit statistics among the fitted models. These results illustrate the practical benefit of the extension while showing that its additional flexibility need not be preferred by every selection criterion.

The main objective of this study is to develop a more flexible extension of the Hj distribution that is capable of effectively modeling complex lifetime data by providing greater control over the shapes of both the PDF and the HRF. The main contributions of this study can be summarized as follows.

- A new version of the Hj distribution is proposed within a competing risks framework, providing enhanced modeling flexibility along with a clear structural interpretation.
- The main structural functions of the model are derived and interpreted in terms of the underlying failure mechanisms. The shapes of the HRF are also investigated, illustrating the ability of the model to accommodate different hazard rate behaviors.
- Several important statistical properties, including moments, entropy measures, and order statistics, are investigated. The quantile function is characterized through an equation that can be solved numerically. In addition, the effects of the model's parameters on its distributional characteristics, particularly skewness and kurtosis, are examined.
- The unknown parameters are estimated using the maximum likelihood method. Bayesian estimation is also developed under independent gamma priors and the squared error loss function, with posterior inference performed using Markov chain Monte Carlo (MCMC) techniques.
- A simulation study is conducted under two parameter configurations and different sample sizes to evaluate the finite-sample performance and estimation accuracy of the proposed estimators.
- The practical applicability of the proposed model is illustrated through the analysis of real datasets and comparisons with competing lifetime distributions.

The remainder of this paper is organized as follows. In Section 2, the GHj distribution is introduced. Section 3 is devoted to studying the main structural properties of the proposed model. In Section 4, the estimation procedures for the unknown parameters are developed under both classical and Bayesian frameworks. A simulation study is presented in Section 5. In Section 6, the practical applicability of the proposed model is illustrated through the analysis of real datasets and comparisons with competing models. Finally, the main conclusions of the study are summarized in Section 7.

2. The GHj distribution

In this section, the GHj distribution is introduced in detail. The main structural functions of the model, including the PDF, CDF, RF, and HRF, are presented and discussed. Particular attention is given to the formulation and interpretation of these functions within the proposed framework. In addition, the behavior of the GHj distribution is explored through graphical illustrations. Various shapes of the HRF are displayed to demonstrate the flexibility of the model in capturing different hazard rate shapes under different parameter settings.

2.1. Formulation of the GHj distribution

Let X_L be a random variable following the Lomax distribution with shape parameter $\alpha > 0$, whose RF is given by

$$R_L(x) = (1 + x)^{-\alpha}, \quad x > 0.$$

Let X_W be a random variable following the Weibull distribution with rate parameter $\lambda > 0$ and shape parameter $\beta > 0$, with RF

$$R_W(x) = \exp\left(-\lambda x^{\beta}\right), \quad x > 0.$$

Assume that X_L and X_W are independent. Under the competing risks framework, the system's lifetime is defined as the minimum of the component lifetimes. Accordingly, let $X = \min(X_L, X_W)$ denote the time to first failure. Due to independence, the RF of X is obtained as the product of the individual RFs:

$$\begin{aligned} R(x) &= P(X > x) \\ &= P(X_L > x)\, P(X_W > x) \\ &= R_L(x)\, R_W(x). \end{aligned} \tag{2.1}$$

Substituting the expressions of $R_L(x)$ and $R_W(x)$ into (2.1), the RF of the GHj distribution is obtained as follows:

$$R(x;\boldsymbol{\theta}) = \frac{e^{-\lambda x^{\beta}}}{(1 + x)^{\alpha}}, \quad x > 0, \quad \lambda, \alpha, \beta > 0, \tag{2.2}$$

where $\boldsymbol{\theta} = (\lambda, \alpha, \beta)^{\top}$. The corresponding CDF is given by

$$F(x;\boldsymbol{\theta}) = 1 - \frac{e^{-\lambda x^{\beta}}}{(1 + x)^{\alpha}}. \tag{2.3}$$

Differentiating (2.3) with respect to x, the PDF of the GHj distribution is obtained follows:

$$f(x;\boldsymbol{\theta}) = \frac{\alpha + \lambda\beta(1 + x)x^{\beta-1}}{(1 + x)^{\alpha+1}} e^{-\lambda x^{\beta}}, \quad x > 0. \tag{2.4}$$

The HRF is defined as

$$h(x;\boldsymbol{\theta}) = \frac{f(x;\boldsymbol{\theta})}{R(x;\boldsymbol{\theta})} = \frac{\alpha}{1 + x} + \lambda\beta x^{\beta-1}. \tag{2.5}$$

It is important to note that the HRF admits a convenient additive decomposition, $h(x) = h_L(x) + h_W(x)$, where $h_L(x) = \frac{\alpha}{1+x}$ is the HRF of the Lomax distribution and $h_W(x) = \lambda\beta x^{\beta-1}$ is the HRF of the Weibull distribution. This decomposition arises naturally from the independence assumption in the

competing risks framework and provides a clear interpretation of the overall hazard as the sum of the cause-specific hazard rates.

It is worth noting that several well-known distributions arise as special cases of the GHj distribution for particular choices of the parameter vector $\boldsymbol{\theta} = (\lambda, \alpha, \beta)^\top$. In particular, the classical Hj distribution is obtained by setting $\beta = 2$ and replacing λ with $\lambda/2$. The Lomax distribution is recovered when $\lambda \to 0^+$, whereas the Weibull distribution is obtained by letting $\alpha \to 0^+$. Further reductions include the exponential distribution, which arises when $\beta = 1$ and $\alpha \to 0^+$, and the Rayleigh distribution, obtained when $\beta = 2$ and $\alpha \to 0^+$ with an appropriate reparameterization of λ. In addition, setting $\beta = 1$ yields a Lomax–exponential –type distribution as a new two-parameter model. These special cases clearly demonstrate the flexibility and generality of the GHj distribution, as it encompasses several classical lifetime models within a unified framework, making it well suited for modeling a wide variety of lifetime data in reliability and survival analysis.

Figure 1 illustrates the PDF of the GHj distribution for nine selected combinations of α and β, with the rate parameter fixed at $\lambda = 1$. The panels display decreasing densities, densities with an interior peak, and nonmonotonic densities exhibiting an initial decrease followed by an increase and a final decrease. These examples illustrate how the density profile varies with α and β, without providing a complete analytical classification of the possible PDF shapes.

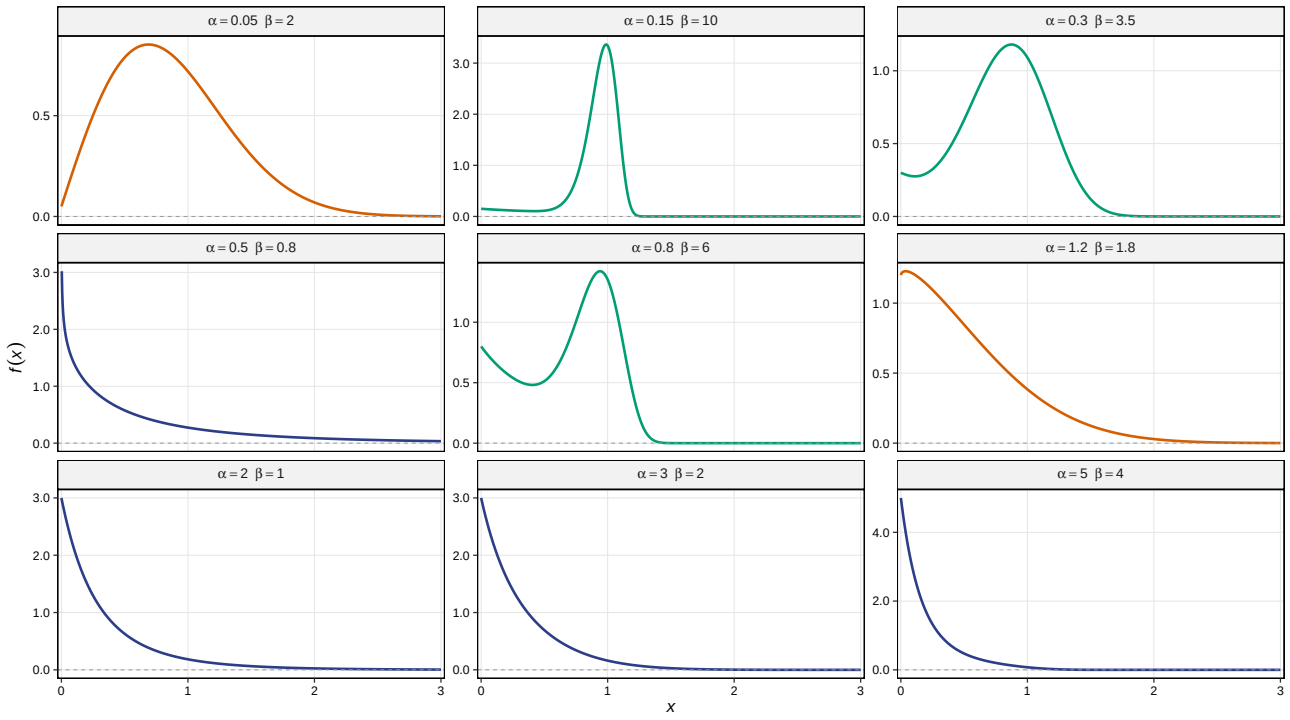


Figure 1. Illustrative shapes of the GHj PDF under different parameter configurations with $\lambda = 1$.

2.2. Shape properties of the HRF

The HRF in (2.5) admits the additive representation

$$h(x;\boldsymbol{\theta}) = \underbrace{\frac{\alpha}{1+x}}_{h_L(x)} + \underbrace{\lambda\beta x^{\beta-1}}_{h_W(x)}, \qquad x > 0, \tag{2.6}$$

where $\lambda, \alpha, \beta > 0$. The Lomax component $h_L(x)$ is strictly decreasing, whereas the Weibull component $h_W(x)$ is decreasing, constant, or increasing according to whether $\beta < 1$, $\beta = 1$, or $\beta > 1$, respectively. Differentiating (2.6) gives

$$h'(x;\boldsymbol{\theta}) = -\frac{\alpha}{(1+x)^2} + \lambda\beta(\beta-1)x^{\beta-2}. \tag{2.7}$$

Define $\rho = \alpha/\lambda$ and

$$g(x) = \beta(\beta-1)x^{\beta-2}(1+x)^2, \qquad x > 0. \tag{2.8}$$

Then

$$h'(x;\boldsymbol{\theta}) = \frac{\lambda}{(1+x)^2}\left[g(x) - \rho\right].$$

Since $\lambda/(1+x)^2 > 0$, the sign of h' is determined by $g(x)-\rho$, and the stationary points satisfy $g(x) = \rho$. For $\beta > 1$, the function g is positive and its logarithmic derivative is

$$\frac{g'(x)}{g(x)} = \frac{\beta-2}{x} + \frac{2}{1+x} = \frac{\beta x + \beta - 2}{x(1+x)}. \tag{2.9}$$

The resulting classification is obtained by considering the following cases.

(i) $0 < \beta < 1$. Both terms in (2.7) are negative, so $h'(x) < 0$ for every $x > 0$. Thus, the HRF is strictly decreasing, with $h(0^+) = +\infty$ and $\lim_{x\to\infty} h(x) = 0$.

(ii) $\beta = 1$. In this case, we have

$$h(x;\boldsymbol{\theta}) = \frac{\alpha}{1+x} + \lambda, \qquad h'(x;\boldsymbol{\theta}) = -\frac{\alpha}{(1+x)^2} < 0.$$

The HRF is strictly decreasing from $\alpha + \lambda$ to λ.

(iii) $1 < \beta < 2$. Here, $g(0^+) = +\infty$ and $\lim_{x\to\infty} g(x) = +\infty$. Equation (2.9) shows that g is strictly decreasing for $x < x_0$ and strictly increasing for $x > x_0$, where

$$x_0 = \frac{2-\beta}{\beta}.$$

Therefore, g has a unique minimum with the value

$$g_{\min}(\beta) = g(x_0) = \frac{4(\beta-1)(2-\beta)^{\beta-2}}{\beta^{\beta-1}}. \tag{2.10}$$

The HRF shape depends on ρ as follows.

- If $\rho < g_{\min}(\beta)$, then $h'(x) > 0$ for every $x > 0$, and the HRF is strictly increasing.
- If $\rho = g_{\min}(\beta)$, then $h'(x) \geq 0$, with equality only at x_0, so the HRF remains strictly increasing. Moreover, $g'(x_0) = 0$ and $g''(x_0) > 0$, giving

$$h''(x_0) = 0, \qquad h'''(x_0) = \frac{\lambda g''(x_0)}{(1 + x_0)^2} > 0.$$

  Hence, x_0 is a stationary inflection point.
- If $\rho > g_{\min}(\beta)$, the equation $g(x) = \rho$ has exactly two solutions, $0 < x_1 < x_0 < x_2$. The derivative satisfies

$$h'(x) > 0 \quad \text{for } x \in (0, x_1) \cup (x_2, \infty), \qquad h'(x) < 0 \quad \text{for } x \in (x_1, x_2).$$

  Thus, the HRF has a local maximum at x_1 and a local minimum at x_2, producing an increase–decrease–increase pattern.

In all three cases, $h(0^+) = \alpha$ and $\lim_{x\to\infty} h(x) = +\infty$.

(iv) $\beta = 2$. The HRF and its derivative become

$$h(x; \boldsymbol{\theta}) = \frac{\alpha}{1 + x} + 2\lambda x, \qquad h'(x; \boldsymbol{\theta}) = \lambda \left[2 - \frac{\rho}{(1 + x)^2}\right].$$

If $\rho < 2$, the derivative is positive for every $x > 0$, so the HRF is strictly increasing. If $\rho = 2$, the derivative is also positive on $(0, \infty)$, but its limit at zero is zero; the continuous extension of the HRF therefore has a horizontal tangent at the origin. If $\rho > 2$, there is a unique stationary point

$$x^* = \sqrt{\frac{\rho}{2}} - 1 = \sqrt{\frac{\alpha}{2\lambda}} - 1 > 0.$$

The derivative is negative for $0 < x < x^*$ and positive for $x > x^*$, yielding a bathtub-shaped HRF.

(v) $\beta > 2$. Equation (2.9) implies that g is strictly increasing, with $g(0^+) = 0$ and $\lim_{x\to\infty} g(x) = +\infty$. For every $\rho > 0$, the equation $g(x) = \rho$ therefore has a unique solution $x^* > 0$. Since

$$h'(x) < 0 \quad \text{for } 0 < x < x^*, \qquad h'(x) > 0 \quad \text{for } x > x^*,$$

the HRF is bathtub-shaped, with a unique minimum at x^*.

The endpoint limits are

$$\lim_{x\to 0^+} h(x; \boldsymbol{\theta}) = \begin{cases} +\infty, & 0 < \beta < 1, \\ \alpha + \lambda, & \beta = 1, \\ \alpha, & \beta > 1, \end{cases} \qquad \lim_{x\to\infty} h(x; \boldsymbol{\theta}) = \begin{cases} 0, & 0 < \beta < 1, \\ \lambda, & \beta = 1, \\ +\infty, & \beta > 1. \end{cases}$$

Table 1 summarizes the classification in terms of $\rho = \alpha/\lambda$ and β. For strictly positive parameters, the HRF can be decreasing, increasing, bathtub-shaped, or increasing–decreasing–increasing. A constant HRF is obtained only in the boundary case $\beta = 1$ and $\alpha \to 0^+$, where $h(x; \boldsymbol{\theta}) \to \lambda$, corresponding to an

exponential distribution with a rate λ. Figure 2 illustrates the supported shapes for selected values of α and β, with $\lambda = 1$ fixed for the graphical presentation.

Table 1. Shape classification of the GHj HRF, where $\rho = \alpha/\lambda$.

β range	ρ range	Shape of $h(x)$
$0 < \beta \leq 1$	Any $\rho > 0$	Strictly decreasing
	$\rho < g_{\min}(\beta)$	Strictly increasing
$1 < \beta < 2$	$\rho = g_{\min}(\beta)$	Strictly increasing with stationary inflection
	$\rho > g_{\min}(\beta)$	Increasing $\rightarrow$ Decreasing $\rightarrow$ Increasing
	$\rho < 2$	Strictly increasing
$\beta = 2$	$\rho = 2$	Strictly increasing; horizontal tangent at origin
	$\rho > 2$	Bathtub-shaped
$\beta > 2$	Any $\rho > 0$	Bathtub-shaped

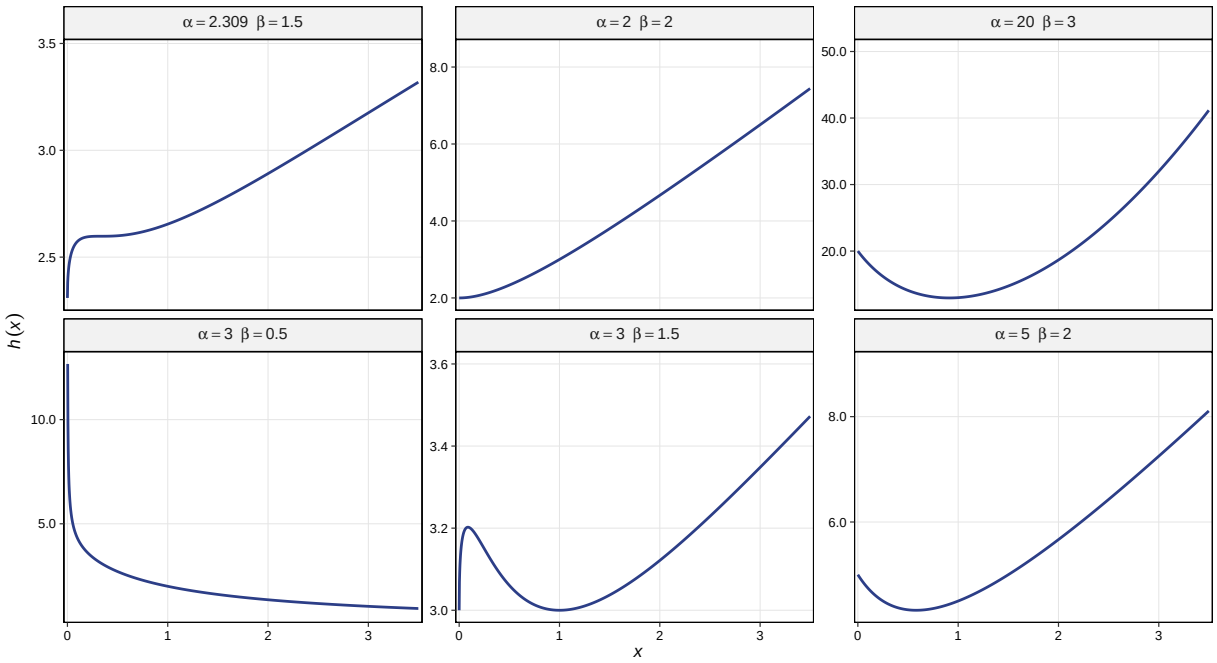


Figure 2. Illustrative shapes of the GHj HRF under different parameter configurations with $\lambda = 1$.

3. Some properties of GHj distribution

In this section, several important properties of the GHj distribution are investigated. In particular, we consider random variate generation and study the moments, order statistics, Rényi entropy, and stress–strength reliability. These properties provide useful theoretical and computational tools for studying the proposed distribution and for its implementation in simulation and inferential procedures.

3.1. Random variate generation

The quantile function of the GHj distribution does not admit a closed-form expression, as it is defined implicitly through the equation

$$\lambda x^{\beta} + \alpha \ln(1 + x) = -\ln(1 - u), \qquad u \in (0, 1).$$

Although numerical root-finding techniques can be used to evaluate the quantile function, such approaches are computationally demanding and may be inefficient for large-scale simulation studies.

An efficient alternative for random variate generation can be obtained by exploiting the competing risks representation of the GHj distribution, see Hjorth [10]. Specifically, let $X = \min(X_L, X_W)$, where $X_L \sim \text{Lomax}(\alpha)$ and $X_W \sim \text{Weibull}(\lambda, \beta)$ are independent random variables. The generation procedure is then given as follows:

1. Generate $U_1, U_2 \sim U(0, 1)$ independently.
2. Set $X_L = (1 - U_1)^{-1/\alpha} - 1$.
3. Set $X_W = \left[-\log(1 - U_2)/\lambda\right]^{1/\beta}$.
4. Define $X = \min(X_L, X_W)$.

Alternatively, noting that $-\log(1 - U_2) \sim \text{Exp}(1)$, one may generate $V \sim \text{Exp}(1)$ and compute $X_W = (V/\lambda)^{1/\beta}$. This procedure avoids numerical inversion and relies only on simple transformations, making it particularly suitable for efficient large-scale simulation.

3.2. Moments

The rth moment about the origin is defined as follows:

$$\mu'_r = \mathbb{E}(X^r) = \int_0^{\infty} x^r f(x; \boldsymbol{\theta})\, dx, \qquad r > 0. \tag{3.1}$$

Substituting the PDF from (2.4) gives

$$\mu'_r = \int_0^{\infty} x^r \frac{\alpha + \lambda\beta(1 + x)x^{\beta-1}}{(1 + x)^{\alpha+1}} e^{-\lambda x^{\beta}}\, dx.$$

For $\alpha, \beta, \lambda > 0$, the integrand satisfies

$$x^r f(x; \boldsymbol{\theta}) = \begin{cases} O(x^{r+\beta-1}), & 0 < \beta < 1, \\ O(x^r), & \beta \geq 1, \end{cases} \qquad x \to 0^+.$$

These expressions are integrable near zero because $r > 0$ and $\beta > 0$. As $x \to \infty$,

$$x^r f(x; \boldsymbol{\theta}) = O\left(x^{r+\beta-\alpha-1} e^{-\lambda x^{\beta}}\right).$$

For every $\lambda, \beta > 0$, the factor $e^{-\lambda x^{\beta}}$ decays faster than any inverse power of x, ensuring integrability at infinity. Thus, every positive-order moment is finite for all $\alpha, \beta, \lambda > 0$.

A simpler representation follows from $f(x;\boldsymbol{\theta}) = -R'(x;\boldsymbol{\theta})$. Integration by parts over $[\varepsilon, M]$, where $0 < \varepsilon < M < \infty$, yields

$$\int_{\varepsilon}^{M} x^r f(x;\boldsymbol{\theta})\,dx = \varepsilon^r R(\varepsilon;\boldsymbol{\theta}) - M^r R(M;\boldsymbol{\theta}) + r\int_{\varepsilon}^{M} x^{r-1} R(x;\boldsymbol{\theta})\,dx.$$

Since $x^r R(x;\boldsymbol{\theta}) \to 0$ at both endpoints, letting $\varepsilon \downarrow 0$ and $M \uparrow \infty$ and applying monotone convergence to the non-negative integrands gives

$$\mu'_r = r\int_0^{\infty} x^{r-1} R(x;\boldsymbol{\theta})\,dx.$$

Substituting $R(x;\boldsymbol{\theta}) = (1+x)^{-\alpha} e^{-\lambda x^{\beta}}$ therefore gives

$$\mu'_r = r\int_0^{\infty} \frac{x^{r-1} e^{-\lambda x^{\beta}}}{(1+x)^{\alpha}}\,dx. \tag{3.2}$$

Moreover, $(1+x)^{-\alpha} \le 1$ implies

$$0 < \mu'_r \le r\int_0^{\infty} x^{r-1} e^{-\lambda x^{\beta}}\,dx = \lambda^{-r/\beta}\Gamma\left(1+\frac{r}{\beta}\right) < \infty.$$

Finally, the substitution $u = \lambda x^{\beta}$ in (3.2) yields

$$\mu'_r = \frac{r}{\beta}\lambda^{-r/\beta}\int_0^{\infty} u^{r/\beta-1}\left[1+\left(\frac{u}{\lambda}\right)^{1/\beta}\right]^{-\alpha} e^{-u}\,du. \tag{3.3}$$

Both (3.2) and (3.3) are exact, absolutely convergent integral representations, and can be evaluated using numerical quadrature. No additional restriction relating α to r or β is required when $\lambda > 0$. At the boundary value $\lambda = 0$, the distribution reduces to the Lomax distribution, whose rth moment is finite if and only if $\alpha > r$.

Figure 3 presents a comprehensive visualization of the mean, variance, skewness, and kurtosis of the GHj distribution as functions of the shape parameters α and β, with the rate parameter fixed at $\lambda = 1$. These quantities were calculated by numerical integration of the raw-moment formula in (3.1) and checked against those obtained from (3.3), with agreement within numerical precision. The plots are constructed over a grid of parameter values to illustrate the sensitivity of these summary measures to changes in the model's parameters. The figure reveals several important features of the GHj distribution. The mean and variance exhibit smooth variation with respect to both parameters, with larger values typically associated with smaller β and moderate values of α. The skewness surface indicates that the distribution is generally positively skewed, particularly for small values of β, while the degree of skewness decreases as β increases. The kurtosis plot demonstrates the presence of heavy-tailed behavior in certain regions of the parameter space, especially when both α and β are relatively small, with the tail heaviness diminishing as β increases. Overall, these graphical results highlight the flexibility of the GHj distribution in capturing a wide range of distributional shapes, confirming its suitability for modeling diverse lifetime data structures.

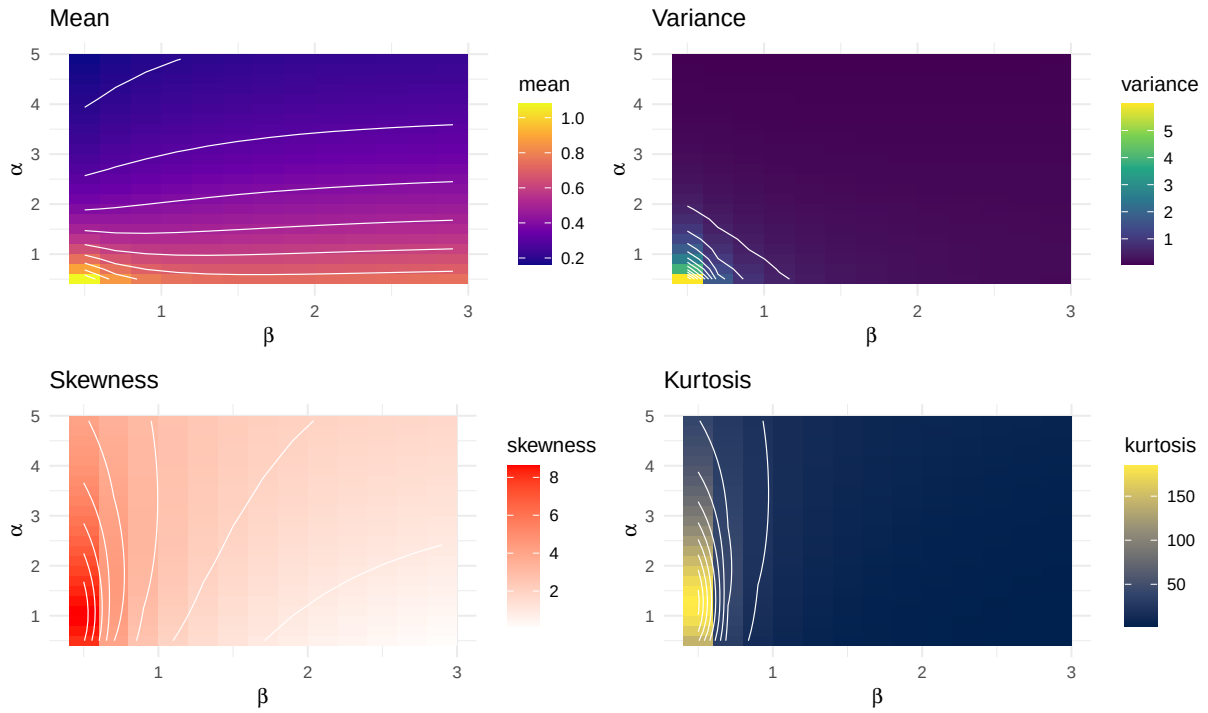


Figure 3. Surface plots of the mean, variance, skewness, and kurtosis of the GHj distribution as functions of the shape parameters α and β, with $\lambda = 1$.

3.3. Order statistics

Let $X_1, X_2, \ldots, X_n$ be independent and identically distributed random variables following the GHj distribution with CDF $F(x)$ and PDF $f(x)$ given in (2.3) and (2.4), respectively. Let $X_{(1)} \leq X_{(2)} \leq \cdots \leq X_{(n)}$ denote the corresponding order statistics. The PDF of $X_{(i)}$ is given by

$$f_{X_{(i)}}(x) = \frac{n!}{(i-1)!\,(n-i)!}[F(x)]^{i-1}[1-F(x)]^{n-i}f(x), \qquad x > 0.$$

Substituting the GHj forms of $F(x)$ and $1 - F(x)$ yields

$$f_{X_{(i)}}(x) = \frac{n!}{(i-1)!\,(n-i)!}\left[1 - \frac{e^{-\lambda x^\beta}}{(1+x)^\alpha}\right]^{i-1}\left[\frac{e^{-\lambda x^\beta}}{(1+x)^\alpha}\right]^{n-i} f(x).$$

Applying the binomial expansion and simplifying, we obtain

$$f_{X_{(i)}}(x) = \frac{n!}{(i-1)!\,(n-i)!}\sum_{j=0}^{i-1}\binom{i-1}{j}(-1)^j \frac{\alpha + \lambda\beta(1+x)x^{\beta-1}}{(1+x)^{\alpha(n-i+j+1)+1}}\, e^{-\lambda(n-i+j+1)x^\beta}, \qquad x > 0. \tag{3.4}$$

The CDF of $X_{(i)}$ is given by

$$F_{X_{(i)}}(x) = \sum_{r=i}^{n}\binom{n}{r}[F(x)]^r[1-F(x)]^{n-r}, \qquad x > 0.$$

Substituting the GHj expressions and applying the binomial expansion lead to

$$F_{X_{(i)}}(x) = \sum_{r=i}^{n} \sum_{j=0}^{r} \binom{n}{r}\binom{r}{j}(-1)^j \frac{e^{-\lambda(n-r+j)x^\beta}}{(1+x)^{\alpha(n-r+j)}}, \qquad x > 0. \tag{3.5}$$

The minimum and maximum order statistics are obtained from (3.4) and (3.5) by setting $i = 1$ and $i = n$, respectively. The minimum, $X_{(1)}$, is particularly relevant in reliability analysis, as it represents the time to first failure, whereas the maximum, $X_{(n)}$, is useful in applications involving extreme values. For the minimum, the PDF simplifies to

$$f_{X_{(1)}}(x) = \frac{n\alpha + n\lambda\beta(1+x)x^{\beta-1}}{(1+x)^{\alpha n+1}}\, e^{-n\lambda x^\beta}, \qquad x > 0.$$

Thus, $X_{(1)}$ follows a GHj distribution with updated parameters $X_{(1)} \sim \text{GHj}(n\lambda, n\alpha, \beta)$. The corresponding CDF is

$$F_{X_{(1)}}(x) = 1 - \frac{e^{-n\lambda x^\beta}}{(1+x)^{\alpha n}}, \qquad x > 0.$$

For the maximum, the PDF is given by

$$f_{X_{(n)}}(x) = n \sum_{j=0}^{n-1} \binom{n-1}{j}(-1)^j \frac{\alpha + \lambda\beta(1+x)x^{\beta-1}}{(1+x)^{\alpha(j+1)+1}}\, e^{-\lambda(j+1)x^\beta}, \qquad x > 0.$$

The corresponding CDF is

$$F_{X_{(n)}}(x) = \sum_{j=0}^{n} \binom{n}{j}(-1)^j \frac{e^{-j\lambda x^\beta}}{(1+x)^{\alpha j}}, \qquad x > 0.$$

Remark 3.1. *The GHj distribution exhibits a closure property under minima: The minimum of n independent GHj random variables remains within the GHj family, with parameters α and λ scaled by n, while β remains unchanged. This property is particularly useful in reliability applications. In contrast, the maximum order statistic does not belong to the GHj family, but can be expressed as a finite mixture of GHj-type densities.*

3.4. Rényi entropy

The Rényi entropy of order $\gamma > 0$, $\gamma \neq 1$, is defined as

$$R_\gamma(X) = \frac{1}{1-\gamma} \log J_\gamma, \qquad J_\gamma = \int_0^\infty [f(x;\boldsymbol{\theta})]^\gamma \, dx, \tag{3.6}$$

provided that $J_\gamma < \infty$. Substituting the GHj density from (2.4) gives

$$J_\gamma = \int_0^\infty \frac{\left[\alpha + \lambda\beta(1+x)x^{\beta-1}\right]^\gamma}{(1+x)^{\gamma(\alpha+1)}} e^{-\gamma\lambda x^\beta} \, dx, \tag{3.7}$$

where $\alpha, \beta, \lambda > 0$. To examine convergence at infinity, consider $x \geq 1$. Since $1 + x \leq 2x$ and $\alpha \leq \alpha x^\beta$,

$$\alpha + \lambda\beta(1+x)x^{\beta-1} \leq (\alpha + 2\lambda\beta)x^\beta.$$

Using $(1+x)^{\alpha+1} \geq x^{\alpha+1}$, we obtain

$$f(x;\boldsymbol{\theta}) \leq (\alpha + 2\lambda\beta)x^{\beta-\alpha-1}e^{-\lambda x^{\beta}},$$

and therefore

$$[f(x;\boldsymbol{\theta})]^{\gamma} \leq (\alpha + 2\lambda\beta)^{\gamma}x^{\gamma(\beta-\alpha-1)}e^{-\gamma\lambda x^{\beta}}.$$

The exponential factor decays faster than any inverse power of x, ensuring that the integral over $(1,\infty)$ is finite for every $\gamma > 0$. Near zero, if $\beta \geq 1$, then $f(x;\boldsymbol{\theta}) \leq \alpha + 2\lambda\beta$ for $0 < x < 1$, so the integral over $(0,1)$ is finite. If $0 < \beta < 1$, then

$$c_1 x^{\beta-1} \leq f(x;\boldsymbol{\theta}) \leq c_2 x^{\beta-1}, \qquad 0 < x < 1,$$

where

$$c_1 = \lambda\beta\, 2^{-(\alpha+1)}e^{-\lambda} > 0, \qquad c_2 = \alpha + 2\lambda\beta > 0.$$

Raising these inequalities to the positive power γ gives

$$c_1^{\gamma}x^{\gamma(\beta-1)} \leq [f(x;\boldsymbol{\theta})]^{\gamma} \leq c_2^{\gamma}x^{\gamma(\beta-1)}.$$

Thus, the integral over $(0,1)$ is finite if and only if

$$\int_0^1 x^{\gamma(\beta-1)}\,dx < \infty,$$

or, equivalently, $\gamma(1-\beta) < 1$. At equality, the integral diverges logarithmically. Combining the behavior at both endpoints, $J_\gamma < \infty$ if and only if $\gamma(1-\beta) < 1$. This condition holds for every $\beta > 0$ when $0 < \gamma < 1$. For $\gamma > 1$, it is equivalent to $\beta > 1 - 1/\gamma$. Consequently, we have

$$R_\gamma(X) = \frac{\log J_\gamma}{1-\gamma}, \qquad \gamma > 0, \quad \gamma \neq 1, \quad \gamma(1-\beta) < 1,$$

with J_γ given in (3.7). If $\gamma > 1$ and $\beta \leq 1 - 1/\gamma$, then $J_\gamma = \infty$ and the Rényi entropy equals $-\infty$ in the extended sense.

The integral in (3.7) can be evaluated numerically without expanding the numerator or the exponential factor. For $\beta \geq 1$, the integrand is bounded near zero. For $0 < \beta < 1$ within the convergence region, define

$$\kappa = 1 - \gamma(1-\beta) \in (0,1), \qquad \widetilde{g}(x) = x^{\gamma(1-\beta)}[f(x;\boldsymbol{\theta})]^{\gamma}.$$

The substitution $x = t^{1/\kappa}$ yields

$$J_\gamma = \frac{1}{\kappa}\int_0^{\infty} \widetilde{g}\left(t^{1/\kappa}\right)\,dt. \tag{3.8}$$

Since

$$\lim_{x\to 0^+}\widetilde{g}(x) = (\lambda\beta)^{\gamma},$$

the transformed integrand has a finite limit at zero and can be extended continuously there. This transformation removes the integrable singularity at the origin and provides an alternative representation for numerical quadrature.

To illustrate the dependence of the entropy on the shape parameters, Figure 4 displays the Rényi entropy for $\gamma = 0.5$ and $\gamma = 2$ as functions of α and β, with $\lambda = 1$. The parameter grids satisfy the convergence condition, which requires $\beta > 0$ for $\gamma = 0.5$ and $\beta > 0.5$ for $\gamma = 2$. For $\gamma = 0.5$, the entropy generally decreases as α and β increase over the displayed grid, with the largest values occurring when both parameters are small. For $\gamma = 2$, the entropy is predominantly negative, with more negative values occurring near the lower end of the displayed β range. Such negative values are permissible for differential Rényi entropy. The figure illustrates how the variation in entropy with the shape parameters depends on the order γ.

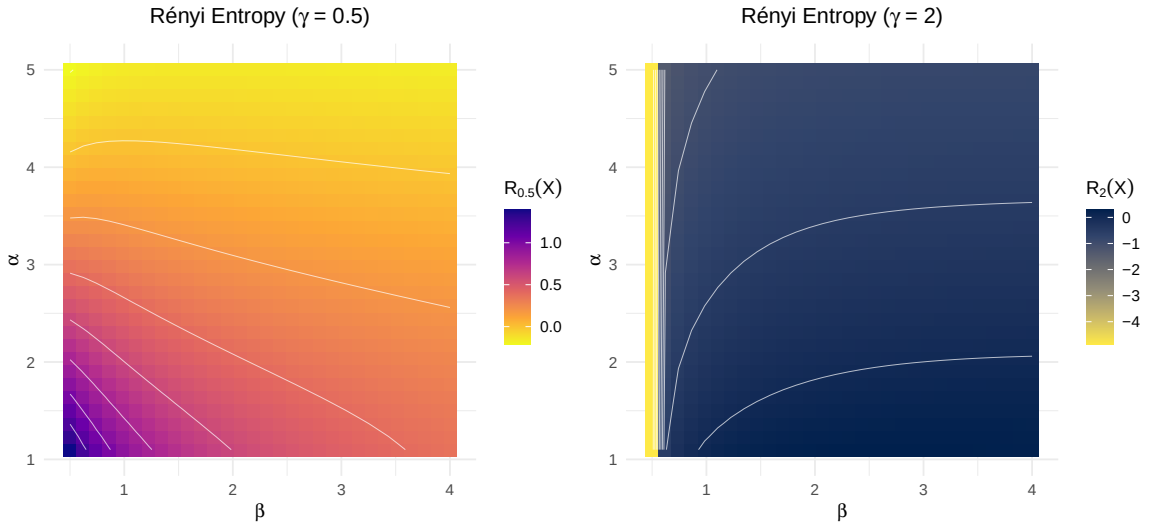


Figure 4. Rényi entropy of the GHj distribution for $\gamma = 0.5$ and $\gamma = 2$ as functions of the shape parameters α and β, with $\lambda = 1$.

3.5. Stress–strength reliability

Let $X_1 \sim \text{GHj}(\lambda_1, \alpha_1, \beta)$ and $X_2 \sim \text{GHj}(\lambda_2, \alpha_2, \beta)$ be independent random variables representing the stress and strength of a component, respectively. The shape parameter $\beta > 0$ is common to both distributions, whereas $\lambda_1, \lambda_2, \alpha_1, \alpha_2 > 0$ may differ. The component operates successfully when the strength exceeds the stress, giving the reliability parameter

$$\mathcal{R} = P(X_2 > X_1) = \int_0^\infty f_{X_1}(x) R_{X_2}(x)\, dx, \tag{3.9}$$

where f_{X_1} is the PDF of the stress and R_{X_2} is the RF of the strength. Substituting the GHj functions from (2.4) and (2.2) yields

$$\mathcal{R} = \int_0^\infty \frac{\alpha_1 + \lambda_1\beta(1+x)x^{\beta-1}}{(1+x)^{\alpha_1+\alpha_2+1}} e^{-(\lambda_1+\lambda_2)x^\beta}\, dx. \tag{3.10}$$

Writing $\alpha^* = \alpha_1 + \alpha_2$ and $\lambda^* = \lambda_1 + \lambda_2$, this expression can be decomposed as

$$\mathcal{R} = \alpha_1 J_1 + \lambda_1\beta J_2, \tag{3.11}$$

where

$$J_1 = \int_0^\infty \frac{e^{-\lambda^* x^\beta}}{(1+x)^{\alpha^*+1}}\, dx, \qquad J_2 = \int_0^\infty \frac{x^{\beta-1} e^{-\lambda^* x^\beta}}{(1+x)^{\alpha^*}}\, dx.$$

Both integrals are finite for all positive parameter values. Near zero, their integrands are asymptotic to 1 and $x^{\beta-1}$, respectively, and are integrable because $\beta > 0$. At infinity, the factor $e^{-\lambda^* x^\beta}$ decays faster than any inverse power of x, ensuring convergence. Thus, no additional restriction relating α^* to β is needed.

The two integrals are related through the RF of $\min(X_1, X_2)$. Differentiation gives

$$-\frac{d}{dx}\left[(1+x)^{-\alpha^*}e^{-\lambda^* x^\beta}\right] = \alpha^*\frac{e^{-\lambda^* x^\beta}}{(1+x)^{\alpha^*+1}} + \lambda^*\beta\frac{x^{\beta-1}e^{-\lambda^* x^\beta}}{(1+x)^{\alpha^*}}.$$

Since the expression inside the derivative tends to one at zero and to zero at infinity, integration yields

$$\alpha^* J_1 + \lambda^*\beta J_2 = 1. \tag{3.12}$$

Using this identity to eliminate J_2 from (3.11) gives

$$\mathcal{R} = \frac{\lambda_1}{\lambda^*} + \frac{\alpha_1\lambda_2 - \alpha_2\lambda_1}{\lambda^*}J_1. \tag{3.13}$$

This representation requires the numerical evaluation of only J_1, whose integrand is bounded near zero for every $\beta > 0$.

Alternatively, setting $u = x^\beta$ in (3.10) gives

$$\mathcal{R} = \int_0^\infty e^{-\lambda^* u}\left[\frac{\alpha_1}{\beta}\frac{u^{1/\beta-1}}{(1+u^{1/\beta})^{\alpha^*+1}} + \frac{\lambda_1}{(1+u^{1/\beta})^{\alpha^*}}\right]du. \tag{3.14}$$

Although this expression is valid for every $\beta > 0$, it is particularly useful when $0 < \beta < 1$: The transformed integrand tends to λ_1 at zero, removing the singularity in (3.10). For $\beta \geq 1$, the original integrand is bounded near zero. These integral representations allow numerical evaluation without a series expansion.

The decomposition also provides an interpretation of $\mathcal{R}$ in terms of the underlying Lomax and Weibull components. Define

$$w = \lambda^*\beta J_2 = 1 - \alpha^* J_1.$$

Since $J_1, J_2 > 0$, (3.12) implies $0 < w < 1$, and (3.11) becomes

$$\mathcal{R} = (1-w)\frac{\alpha_1}{\alpha_1+\alpha_2} + w\frac{\lambda_1}{\lambda_1+\lambda_2}.$$

Thus, $\mathcal{R}$ is a convex combination of the stress–strength probabilities associated with the Lomax components alone and the Weibull components alone. When these probabilities differ, we have

$$\min\left\{\frac{\alpha_1}{\alpha_1+\alpha_2}, \frac{\lambda_1}{\lambda_1+\lambda_2}\right\} < \mathcal{R} < \max\left\{\frac{\alpha_1}{\alpha_1+\alpha_2}, \frac{\lambda_1}{\lambda_1+\lambda_2}\right\}.$$

If $\alpha_1\lambda_2 = \alpha_2\lambda_1$, the two component probabilities coincide. In this case, the GHj hazard rates are proportional and

$$\mathcal{R} = \frac{\alpha_1}{\alpha_1+\alpha_2} = \frac{\lambda_1}{\lambda_1+\lambda_2}.$$

In particular, identical stress and strength distributions, obtained when $\alpha_1 = \alpha_2$ and $\lambda_1 = \lambda_2$, give $\mathcal{R} = 1/2$.

4. Classical and Bayesian estimation

In this section, the unknown parameters of the GHj distribution are estimated using both classical and Bayesian approaches. Maximum likelihood estimation is used for classical inference, while Bayesian estimation is developed under suitable prior assumptions.

4.1. Maximum likelihood estimation

Let $x_1, \ldots, x_n > 0$ be an observed random sample from the GHj distribution with parameter vector $\boldsymbol{\theta} = (\lambda, \alpha, \beta)^\top \in (0, \infty)^3$. Using (2.4), the likelihood function is

$$L(\boldsymbol{\theta}) = \prod_{i=1}^{n} f(x_i; \boldsymbol{\theta}) = \prod_{i=1}^{n} \frac{\psi_i}{(1 + x_i)^{\alpha+1}} e^{-\lambda x_i^{\beta}}, \tag{4.1}$$

where $\psi_i = \alpha + \lambda\beta(1 + x_i)x_i^{\beta-1}, i = 1, \ldots, n$. The corresponding log-likelihood function is

$$l(\boldsymbol{\theta}) = \sum_{i=1}^{n} \log \psi_i - (\alpha + 1) \sum_{i=1}^{n} \log(1 + x_i) - \lambda \sum_{i=1}^{n} x_i^{\beta}. \tag{4.2}$$

Interior stationary points of the log-likelihood satisfy the likelihood equations

$$\frac{\partial l(\boldsymbol{\theta})}{\partial \lambda} = \beta \sum_{i=1}^{n} \frac{(1 + x_i)x_i^{\beta-1}}{\psi_i} - \sum_{i=1}^{n} x_i^{\beta} = 0, \tag{4.3}$$

$$\frac{\partial l(\boldsymbol{\theta})}{\partial \alpha} = \sum_{i=1}^{n} \frac{1}{\psi_i} - \sum_{i=1}^{n} \log(1 + x_i) = 0, \tag{4.4}$$

and

$$\frac{\partial l(\boldsymbol{\theta})}{\partial \beta} = \lambda \sum_{i=1}^{n} \frac{(1 + x_i)x_i^{\beta-1}\left[1 + \beta \log x_i\right]}{\psi_i} - \lambda \sum_{i=1}^{n} x_i^{\beta} \log x_i = 0. \tag{4.5}$$

It should be noted that the unrestricted GHj log-likelihood is unbounded above. In particular, taking $\lambda = x_{(n)}^{-\beta}$ and letting $\beta \to \infty$ yields a degenerate sequence along which the log-likelihood diverges. Therefore, the finite estimates considered here correspond to an interior local maximizer rather than a global unrestricted maximum. Accordingly, the likelihood equations are treated numerically to obtain the finite interior solution considered in this study. Liu and Xue [25] developed high-order iterative methods for nonlinear equation systems, which are relevant to the numerical treatment of likelihood equations arising in parameter estimation.

The boundary behavior of the likelihood requires particular attention. Two meaningful limiting submodels arise from the closure of the parameter space. As $\lambda \to 0^+$ with α and β being fixed, (4.2) tends to

$$l_L(\alpha) = n \log \alpha - (\alpha + 1) \sum_{i=1}^{n} \log(1 + x_i), \tag{4.6}$$

which is the log-likelihood function of the Lomax submodel. Its unique maximizer is

$$\widehat{\alpha}_L = \frac{n}{\sum_{i=1}^{n} \log(1 + x_i)}. \tag{4.7}$$

Similarly, as $\alpha \to 0^+$ with λ and β fixed, (4.2) tends to

$$l_W(\lambda,\beta) = n\log\lambda + n\log\beta + (\beta-1)\sum_{i=1}^{n}\log x_i - \lambda\sum_{i=1}^{n}x_i^{\beta}, \tag{4.8}$$

which is the log-likelihood function of the Weibull submodel. For a fixed $\beta > 0$, its unique maximizer with respect to λ is

$$\widehat{\lambda}_W(\beta) = \frac{n}{\sum_{i=1}^{n}x_i^{\beta}}. \tag{4.9}$$

The finite limiting likelihoods in (4.6) and (4.8) show that the lower boundaries cannot be excluded merely through continuity arguments. In particular, these boundary calculations do not, by themselves, establish the existence of an interior maximizer. Rather than imposing a general existence or uniqueness claim over the complete three-dimensional parameter space, below, we establish a conditional concavity property of the log-likelihood with respect to (λ,α) for fixed β.

Proposition 1. *For fixed $\beta > 0$, define*

$$t_i = \beta(1+x_i)x_i^{\beta-1}, \qquad i = 1,\ldots,n.$$

Then the log-likelihood function $l(\boldsymbol{\theta})$ is concave in $(\lambda,\alpha) \in (0,\infty)^2$. If $t_1,\ldots,t_n$ are not all equal, it is strictly concave. Provided that $t_1,\ldots,t_n$ are not all equal, any interior solution of the conditional score equations is the unique global maximizer of the conditional log-likelihood with respect to (λ,α) for the specified value of β.

Proof. For fixed $\beta > 0$, the Hessian matrix of the log-likelihood with respect to (λ,α) is

$$\mathbf{H}_{(\lambda,\alpha)} = -\sum_{i=1}^{n}\frac{1}{(\alpha+\lambda t_i)^2}\begin{pmatrix}1 & t_i\\ t_i & t_i^2\end{pmatrix}.$$

For any $\mathbf{v} = (v_1,v_2)^{\top} \in \mathbb{R}^2$, we have

$$\mathbf{v}^{\top}\mathbf{H}_{(\lambda,\alpha)}\mathbf{v} = -\sum_{i=1}^{n}\frac{(v_1+t_iv_2)^2}{(\alpha+\lambda t_i)^2} \le 0.$$

Hence, $\mathbf{H}_{(\lambda,\alpha)}$ is negative semidefinite, which establishes concavity of the log-likelihood in (λ,α).

Suppose that $t_1,\ldots,t_n$ are not all equal. Then indices i and j exist such that $t_i \neq t_j$. Equality in the preceding quadratic form requires

$$v_1 + t_rv_2 = 0, \qquad r = 1,\ldots,n.$$

In particular, we have

$$v_1 + t_iv_2 = 0 \qquad \text{and} \qquad v_1 + t_jv_2 = 0.$$

Subtracting these equations gives

$$(t_i - t_j)v_2 = 0.$$

Since $t_i \neq t_j$, it follows that $v_2 = 0$, and, consequently, $v_1 = 0$. Thus, equality occurs only for $\mathbf{v} = \mathbf{0}$, and $\mathbf{H}_{(\lambda,\alpha)}$ is negative definite. Since $(0,\infty)^2$ is a convex domain, strict concavity implies that any interior stationary point is the unique global maximizer of the conditional log-likelihood with respect to (λ,α) for the specified value of β. □

Any interior solution of the conditional score equations also satisfies a useful identity. Multiplying (4.4) by α and (4.3) by λ and adding the resulting equations gives

$$\alpha \sum_{i=1}^{n} \log(1 + x_i) + \lambda \sum_{i=1}^{n} x_i^{\beta} = \sum_{i=1}^{n} \frac{\alpha + \lambda\beta(1 + x_i)x_i^{\beta-1}}{\psi_i} = n.$$

Therefore, we have

$$\alpha \sum_{i=1}^{n} \log(1 + x_i) + \lambda \sum_{i=1}^{n} x_i^{\beta} = n. \tag{4.10}$$

Since both terms on the left-hand side of (4.10) are strictly positive, any interior solution necessarily satisfies

$$0 < \alpha < \frac{n}{\sum_{i=1}^{n} \log(1 + x_i)}, \qquad 0 < \lambda < \frac{n}{\sum_{i=1}^{n} x_i^{\beta}}. \tag{4.11}$$

The upper bounds in (4.11) coincide with the Lomax boundary estimate in (4.7) and the conditional Weibull estimate in (4.9), respectively. These relations provide useful analytical checks for interior numerical solutions but do not, by themselves, establish their existence.

The preceding proposition establishes conditional uniqueness with respect to (λ, α) for fixed β under the stated condition. It does not establish the existence of an interior maximizer or uniqueness with respect to the complete parameter vector $\boldsymbol{\theta}$, since β remains unrestricted in the conditional analysis. Accordingly, no general claim concerning the existence or global uniqueness of an interior maximum likelihood estimator (MLE) is made here. The likelihood equations are solved numerically, with further details concerning the numerical implementation provided in the corresponding numerical sections.

4.2. Bayesian estimation

Bayesian inference provides a flexible and coherent framework for parameter estimation, particularly in complex models where classical methods may face analytical or computational challenges. By incorporating prior information and combining it with the likelihood function, Bayesian methods yield full posterior distributions, allowing for comprehensive uncertainty quantification. For general references on Bayesian inference and its applications; see Bouguila et al. [26], and Zyphur and Oswald [27]. In this part, Bayesian estimation of the unknown parameters of the GHj distribution is developed under the squared error loss function. Inspection of the likelihood function in (4.1) reveals that no conjugate prior exists for the model's parameters. Therefore, to respect the positivity constraints of the parameters and to maintain analytical tractability, independent gamma priors are assumed for each parameter.

Assume that the three unknown parameters are independent. Specifically, let $\lambda \sim \text{gamma}(a_1, b_1)$, $\alpha \sim \text{gamma}(a_2, b_2)$, and $\beta \sim \text{gamma}(a_3, b_3)$, where the hyper-parameters $a_i > 0$ and $b_i > 0$, $i = 1, 2, 3$, are assumed to be known. Then, the joint prior distribution can be written as

$$\pi(\lambda, \alpha, \beta) \propto \lambda^{a_1-1}\alpha^{a_2-1}\beta^{a_3-1}e^{-b_1\lambda-b_2\alpha-b_3\beta}, \qquad \lambda, \alpha, \beta > 0. \tag{4.12}$$

Combining the likelihood function in (4.1) with the joint prior in (4.12), the posterior distribution

of $\boldsymbol{\theta}$ can be expressed as

$$P(\boldsymbol{\theta}|\mathbf{x}) = \frac{\lambda^{a_1-1}\alpha^{a_2-1}\beta^{a_3-1}}{C} \exp\left\{\sum_{i=1}^{n} \log(\psi_i) - \alpha Q - \lambda\left[\sum_{i=1}^{n} x_i^{\beta} + b_1\right] - b_3\beta\right\}, \tag{4.13}$$

where $\mathbf{x} = (x_1, \ldots, x_n)$, $Q = \sum_{i=1}^{n} \log(1 + x_i) + b_2$, and C is the normalized constant.

Under the squared error loss function, the Bayes estimator of any function of the model parameters, say $\phi(\boldsymbol{\theta})$, is given by its posterior mean. However, due to the complexity of the posterior distribution in (4.13), the Bayes estimators cannot be obtained in closed form. Therefore, MCMC methods are used to generate samples from the posterior distribution and approximate the required quantities. To implement the MCMC algorithm, it is necessary to derive the full conditional distributions of the parameters λ, α, and β, respectively, as

$$P_1(\lambda|\alpha,\beta,\mathbf{x}) \propto \lambda^{a_1-1} \exp\left\{\sum_{i=1}^{n} \log(\psi_i) - \lambda\left[\sum_{i=1}^{n} x_i^{\beta} + b_1\right]\right\}, \tag{4.14}$$

$$P_2(\alpha|\lambda,\beta,\mathbf{x}) \propto \alpha^{a_2-1} \exp\left\{\sum_{i=1}^{n} \log(\psi_i) - \alpha Q\right\}, \tag{4.15}$$

and

$$P_3(\beta|\lambda,\alpha,\mathbf{x}) \propto \beta^{a_3-1} \exp\left\{\sum_{i=1}^{n} \log(\psi_i) - \lambda\sum_{i=1}^{n} x_i^{\beta} - b_3\beta\right\}. \tag{4.16}$$

It is evident from (4.14)–(4.16) that the full conditional distributions do not correspond to any standard known forms. To address this difficulty, we use the Metropolis–Hastings (MH) algorithm (see Metropolis et al. [28] and Hastings [29] for more details) to generate samples for λ, α, and β, which are then used to approximate the Bayes estimates. For implementation, a normal distribution is adopted as the proposal distribution for each parameter. The detailed steps of the sampling procedure and the computation of the Bayes estimates are outlined below.

1. Choose the initial values $(\lambda^{(0)}, \alpha^{(0)}, \beta^{(0)})$ and specify the total number of iterations $\mathcal{N}$ and the burn-in period $\mathcal{B}$.

2. Given $(\alpha^{(d-1)}, \beta^{(d-1)})$, generate a candidate $\lambda^{\star}$ from $\lambda^{\star} \sim N(\lambda^{(d-1)}, \sigma_{\lambda}^2)$, where σ_{λ}^2 is the proposal variance, and accept it with probability

$$A_{\lambda} = \min\left\{1, \frac{P_1(\lambda^{\star} \mid \alpha^{(d-1)}, \beta^{(d-1)}, \mathbf{x})}{P_1(\lambda^{(d-1)} \mid \alpha^{(d-1)}, \beta^{(d-1)}, \mathbf{x})}\right\}.$$

   If accepted, set $\lambda^{(d)} = \lambda^{\star}$; otherwise, set $\lambda^{(d)} = \lambda^{(d-1)}$.

3. Given $(\lambda^{(d)}, \beta^{(d-1)})$, generate a candidate $\alpha^{\star}$ from $\alpha^{\star} \sim N(\alpha^{(d-1)}, \sigma_{\alpha}^2)$, and accept it with probability

$$A_{\alpha} = \min\left\{1, \frac{P_2(\alpha^{\star} \mid \lambda^{(d)}, \beta^{(d-1)}, \mathbf{x})}{P_2(\alpha^{(d-1)} \mid \lambda^{(d)}, \beta^{(d-1)}, \mathbf{x})}\right\}.$$

   If accepted, set $\alpha^{(d)} = \alpha^{\star}$; otherwise, set $\alpha^{(d)} = \alpha^{(d-1)}$.

4. Given $(\lambda^{(d)}, \alpha^{(d)})$, generate a candidate $\beta^\star$ using $\beta^\star \sim N(\beta^{(d-1)}, \sigma_\beta^2)$, and accept it with probability

$$A_\beta = \min\left\{1, \frac{P_3(\beta^\star \mid \lambda^{(d)}, \alpha^{(d)}, \mathbf{x})}{P_3(\beta^{(d-1)} \mid \lambda^{(d)}, \alpha^{(d)}, \mathbf{x})}\right\}.$$

   If accepted, set $\beta^{(d)} = \beta^\star$; otherwise, set $\beta^{(d)} = \beta^{(d-1)}$.

5. Repeat Steps 2–4 for $d = 1, 2, \ldots, \mathcal{N}$ to obtain a Markov chain $(\lambda^{(d)}, \alpha^{(d)}, \beta^{(d)})$.

6. Discard the first $\mathcal{B}$ samples as burn-in and use the remaining samples to approximate the posterior summaries and Bayes estimates.

7. Compute the Bayes estimates as the posterior means based on the retained MCMC samples. For $\mathcal{M} = \mathcal{N} - \mathcal{B}$, we have

$$\tilde{\lambda} = \frac{1}{\mathcal{M}} \sum_{d=\mathcal{B}+1}^{\mathcal{N}} \lambda^{(d)}, \quad \tilde{\alpha} = \frac{1}{\mathcal{M}} \sum_{d=\mathcal{B}+1}^{\mathcal{N}} \alpha^{(d)}, \quad \tilde{\beta} = \frac{1}{\mathcal{M}} \sum_{d=\mathcal{B}+1}^{\mathcal{N}} \beta^{(d)}.$$

5. Simulation study

In this section, a simulation study is conducted to evaluate the performance of both classical and Bayesian estimation methods for the GHj distribution. The primary objective is to examine the estimation accuracy of the proposed estimators under different parameter configurations and varying sample sizes. Two representative sets of model parameters are considered, namely Set I: $\lambda = 0.5$, $\alpha = 0.5$, $\beta = 0.5$, and Set II: $\lambda = 0.8$, $\alpha = 1.5$, $\beta = 1.5$. To investigate the effect of sample size, six sample sizes are examined, specifically $n = 25, 50, 100, 150, 250$, and 500, ranging from relatively small to large samples. For each configuration, 1000 random samples are generated using the algorithm described in Subsection 3.1.

From the classical perspective, the likelihood-based estimates of the unknown parameters are obtained numerically using `R`. For each simulated sample, the negative log-likelihood is minimized using the Newton-type algorithm implemented in `nlm`. To reduce the influence of the initial values and examine the numerical sensitivity of the optimization, eight starting points are considered: $(1, 1, 1)$, $(0.5, 0.5, 0.5)$, $(0.5, 1, 0.1)$, $(1, 0.1, 1)$, $(0.5, 0.1, 0.1)$, $(0.1, 1, 0.5)$, $(0.5, 1, 2)$, and $(1, 2, 0.5)$. The optimization is performed separately from each starting point, with a maximum of 1000 iterations. Candidate solutions are screened according to the convergence status, the magnitude of the scaled score vector, and the positive definiteness of the observed information matrix. In addition, solutions associated with the degenerate sequence arising as $\beta \to \infty$ are excluded from consideration. Among the remaining admissible interior solutions, the one achieving the largest log-likelihood is retained. The solutions obtained from the different starting points are also compared to assess sensitivity to the initialization.

From the Bayesian perspective, inference is carried out under the squared error loss function using the MH algorithm. For each simulated sample, 12,000 MCMC iterations are generated, with the first 2,000 discarded as burn-in. Two prior specifications are considered to examine the effect of prior information. Under Prior 1, the hyper-parameters are selected so that the prior means coincide with the parameter values used to generate the data. For Set I, where $(\lambda, \alpha, \beta) = (0.5, 0.5, 0.5)$,

Prior 1 is specified by $(a_1, b_1) = (1, 2)$, $(a_2, b_2) = (2, 4)$, and $(a_3, b_3) = (2, 4)$. For Set II, where $(\lambda, \alpha, \beta) = (0.8, 1.5, 1.5)$, the corresponding specification is $(a_1, b_1) = (1.6, 2)$, $(a_2, b_2) = (7.5, 5)$, and $(a_3, b_3) = (4.5, 3)$. Prior 2 is specified independently for all three parameters as $gamma(0.01, 0.01)$, using the shape–rate parameterization, and is included to examine the behavior of the Bayesian estimates under substantially weaker prior information. The MH algorithm is initialized at the corresponding MLEs. A normal random-walk proposal centered at the current state is used, with the proposal standard deviations determined from the standard errors (SEs) obtained from the inverse observed information matrix at the fitted solution. A proposed state containing any nonpositive parameter value is rejected and the current state is retained, in accordance with the support $(0, \infty)^3$ of the posterior distribution.

For each combination of parameter set and sample size, 1000 completed Monte Carlo replications are used to evaluate the estimators. The sample sizes are $n = 25, 50, 100, 150, 250,$ and 500. The estimation's accuracy is assessed using the mean absolute bias (MAB) and root mean squared error (RMSE). In addition, the median absolute error (MedAE) is reported as a robust measure that is less sensitive to occasional extreme estimates. The three measures are calculated for the MLE and for the Bayes estimates under Prior 1 and Prior 2. This additional robust summary is particularly useful for distinguishing generally poor estimation from cases in which the RMSE is inflated by a relatively small number of extreme estimates.

To evaluate the performance of the estimators, two commonly used measures are used, namely the mean absolute bias (MAB) and the root mean squared error (RMSE). Let $\hat{\theta}_i^{(j)}$ denote the estimate of a parameter θ_i obtained from the jth simulated sample, $j = 1, \ldots, N$, where $N = 1000$. Then, the MAB and RMSE are defined as

$$\mathrm{MAB}(\hat{\theta}_i) = \frac{1}{N} \sum_{j=1}^{N} \left| \hat{\theta}_i^{(j)} - \theta_i \right|$$

and

$$\mathrm{RMSE}(\hat{\theta}_i) = \sqrt{\frac{1}{N} \sum_{j=1}^{N} \left(\hat{\theta}_i^{(j)} - \theta_i \right)^2}.$$

These measures provide complementary information about the estimator's performance. The MAB quantifies the average deviation from the true parameter value, while the RMSE incorporates both bias and variability, offering an overall measure of estimation accuracy. Smaller values of MAB and RMSE indicate better estimator performance.

Figures 5–7 and 8–10 present heatmaps of the MAB, RMSE, and median absolute error (MedAE) for the two parameter configurations, allowing comparisons across sample sizes and estimation methods. The MedAE provides a robust measure of estimation accuracy that is less sensitive to occasional extreme estimates than the MAB and RMSE.

Estimation accuracy generally improves as the sample size increases under both parameter configurations, although the rate of improvement differs across parameters and estimation methods. The MAB, RMSE, and MedAE exhibit broadly decreasing patterns with increasing n. A noticeable feature of the likelihood-based results is the comparatively large RMSE of $\hat{\beta}$ for small samples, particularly under Set II. The additional MedAE results help clarify this behavior. For example, under Set I at $n = 25$, the MLE of β has an RMSE of 1.391, whereas its MedAE is only 0.153. The corresponding values under Set II are 4.256 and 0.954, respectively. Examination of the simulated

estimates shows that this discrepancy is associated with right-skewed sampling distributions containing occasional extreme estimates of β. Such estimates have a pronounced effect on RMSE because of its squared-error formulation, while MedAE is substantially less affected. The influence of these extreme estimates diminishes markedly as the sample size increases, and the three accuracy measures become considerably smaller for larger samples. Thus, the relatively large small-sample RMSE should not be interpreted as indicating uniformly poor estimation across the simulated samples.

Bayesian estimation under Prior 1 yields smaller MAB, RMSE, and MedAE in many of the investigated cases, particularly for small and moderate sample sizes. This result should, however, be interpreted in light of the prior specification, since the means of Prior 1 coincide with the parameter values used to generate the data and therefore provide favorable prior information. Its better finite-sample performance should not be viewed as showing the general superiority of Bayesian estimation over the MLE. Prior 2 generally produces larger estimation errors for smaller samples, but its performance improves as the sample size increases, and the differences among the estimation methods tend to become less pronounced in several cases. Overall, the results indicate that finite-sample estimation accuracy depends on the parameter configuration, sample size, estimation method, and prior specification. The simulation findings describe finite-sample behavior under the two configurations considered and are not intended to establish consistency or asymptotic efficiency.

To assess the convergence of the MCMC algorithm under Prior 1, several standard diagnostic tools are used, including trace plots, autocorrelation function (ACF) plots, and the Gelman–Rubin shrink factor. All convergence diagnostics are based on 30,000 MCMC iterations, with the first 5,000 iterations discarded as burn-in, using Set I of the model parameters and a sample of size 100. The Gelman–Rubin diagnostic is obtained, based on four independent MCMC chains, and the acceptance rate is approximately 40%. The trace plots, presented in Figure 11, show that the chains for all model parameters are stable and well-mixed, fluctuating around constant mean levels without any noticeable trends or systematic patterns. This behavior indicates that the Markov chains have reached their stationary distributions after the burn-in period. The ACF plots, displayed in Figure 12, exhibit a gradual decay in autocorrelation as the lag increases, suggesting that the dependence between successive samples diminishes at a reasonable rate. This reflects adequate mixing of the chains and supports the efficiency of the sampling procedure. Furthermore, the Gelman–Rubin diagnostic, illustrated in Figure 13, shows that the potential scale reduction factors for all parameters rapidly approach one and remain close to unity throughout the sampling process. This provides strong evidence that convergence has been achieved and that the chains are sampling from the target posterior distribution. Overall, these diagnostic results collectively confirm that the MCMC algorithm performs efficiently under Prior 1, yielding reliable posterior samples suitable for subsequent Bayesian inference.

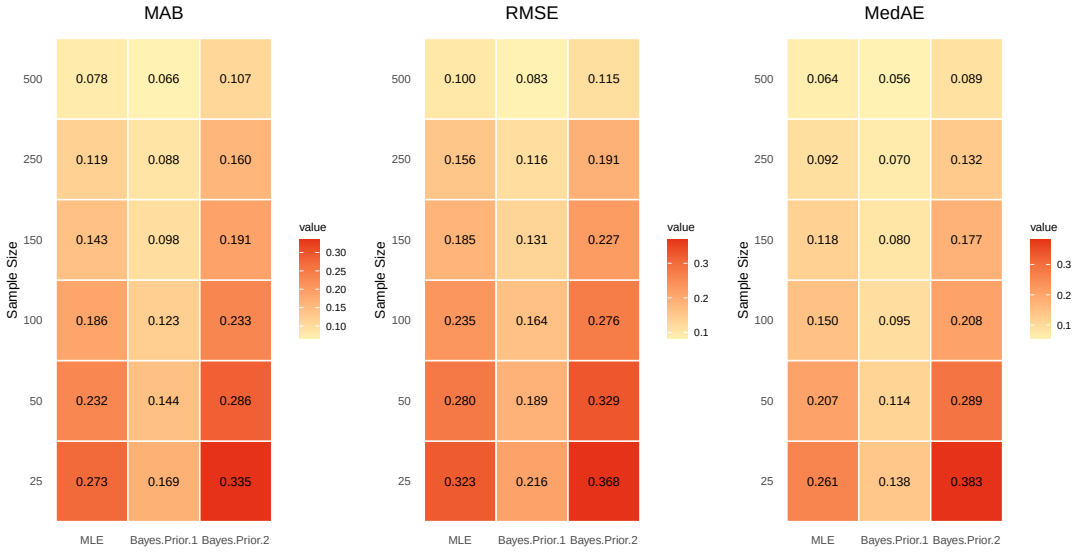


Figure 5. Heatmap representation of MAB, RMSE, and MedAE for the parameter λ under Set I across different sample sizes and estimation methods.

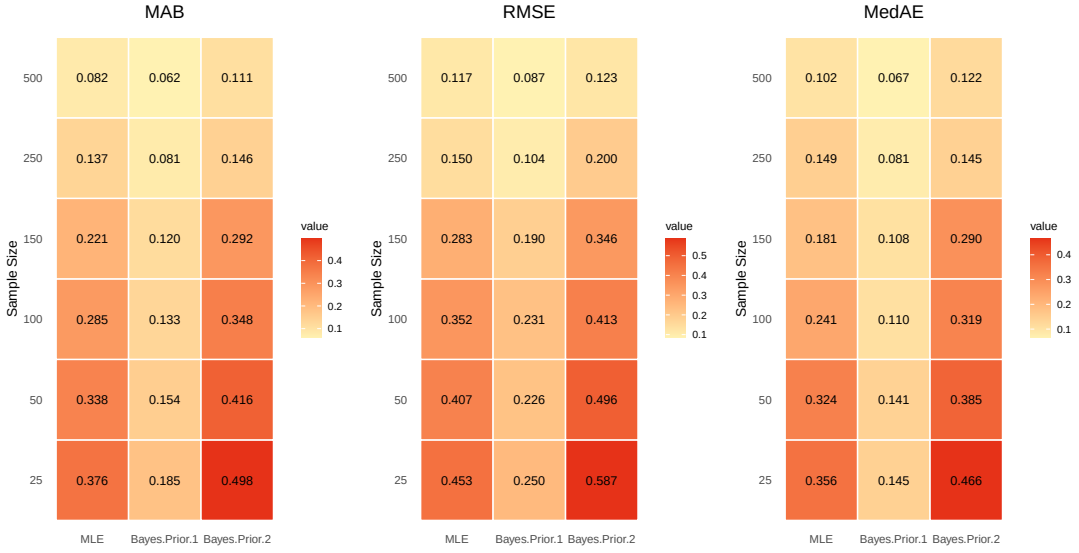


Figure 6. Heatmap representation of MAB, RMSE, and MedAE for the parameter α under Set I across different sample sizes and estimation methods.

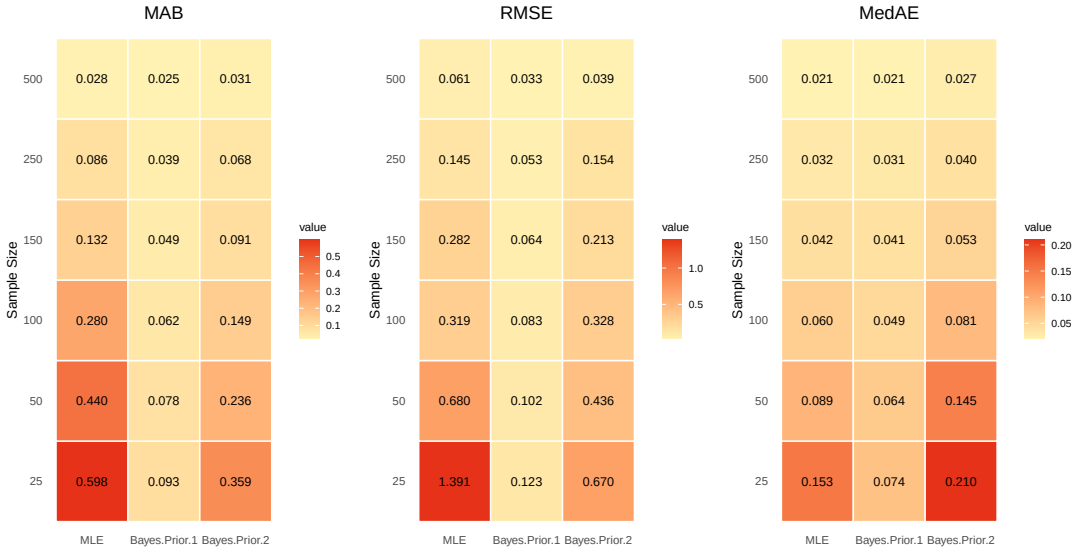


Figure 7. Heatmap representation of MAB, RMSE, and MedAE for the parameter β under Set I across different sample sizes and estimation methods.

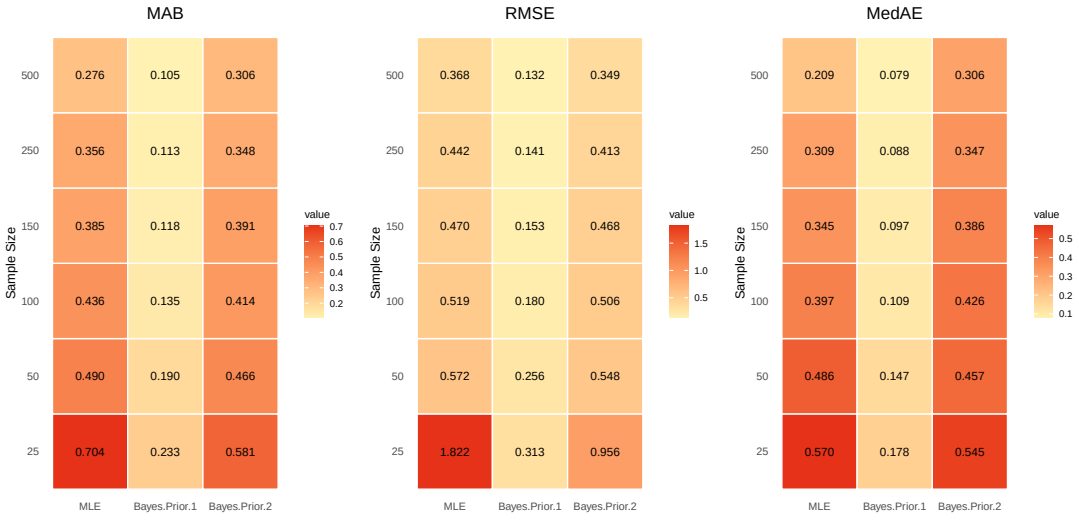


Figure 8. Heatmap representation of MAB, RMSE, and MedAE for the parameter λ under Set II across different sample sizes and estimation methods.

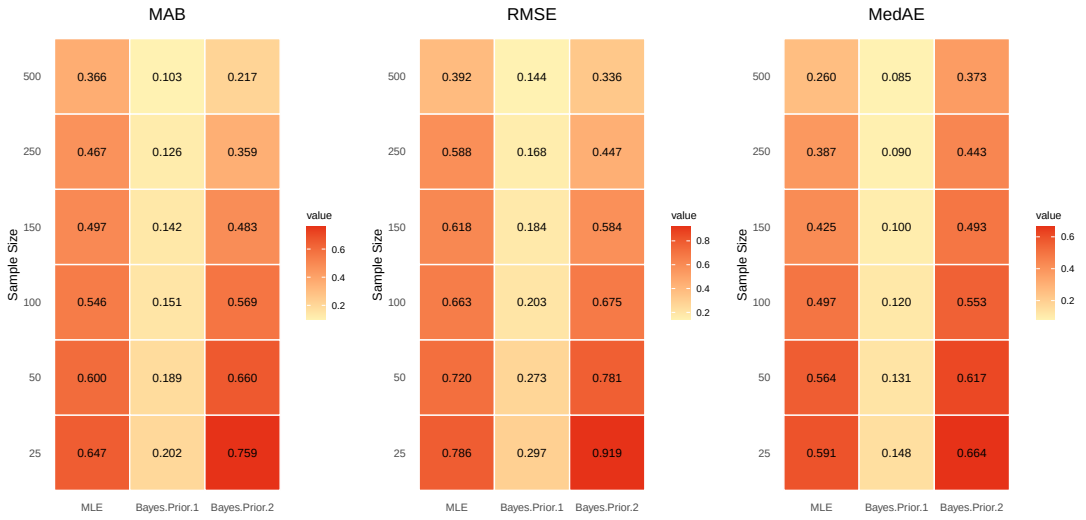


Figure 9. Heatmap representation of MAB, RMSE, and MedAE for the parameter α under Set II across different sample sizes and estimation methods.

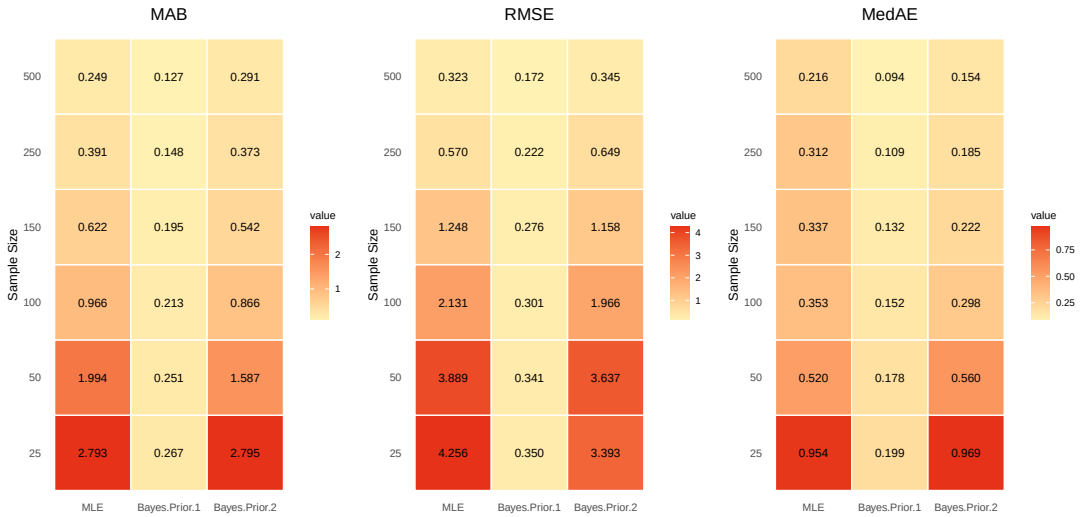


Figure 10. Heatmap representation of MAB, RMSE, and MedAE for the parameter β under Set II across different sample sizes and estimation methods.

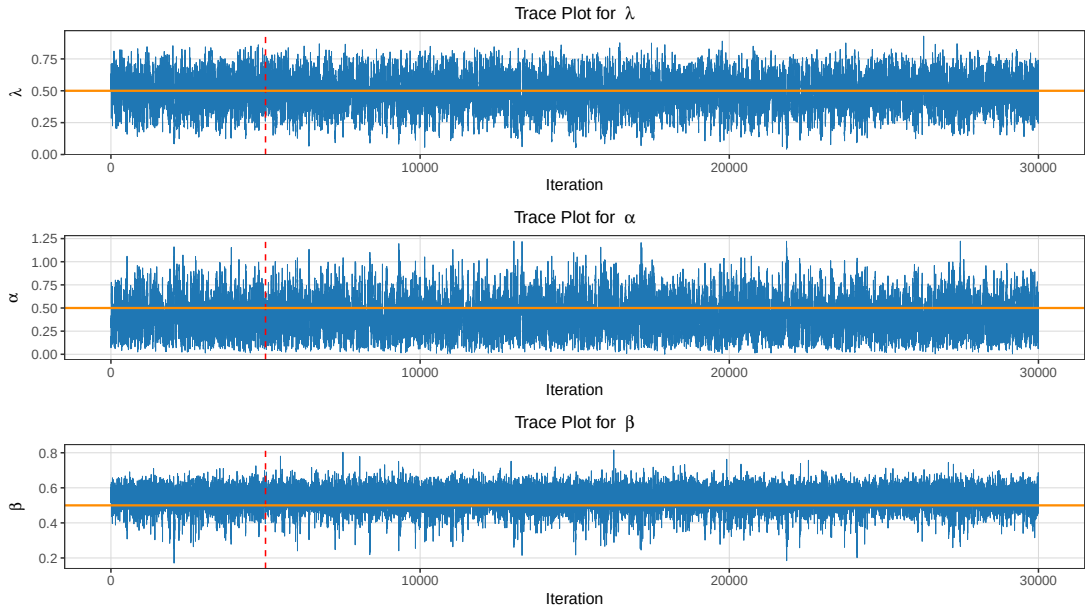


Figure 11. Trace plots for the MCMC samples of the parameters λ, α, and β under Prior 1 based on Set I.

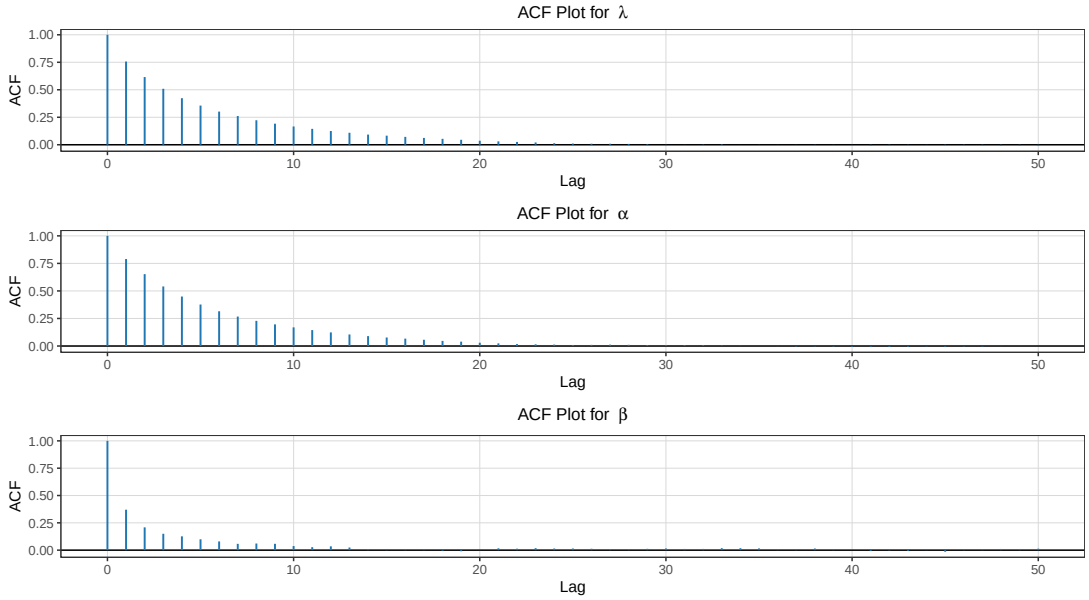


Figure 12. Autocorrelation function plots for the MCMC samples of the parameters λ, α, and β under Prior 1 based on Set I.

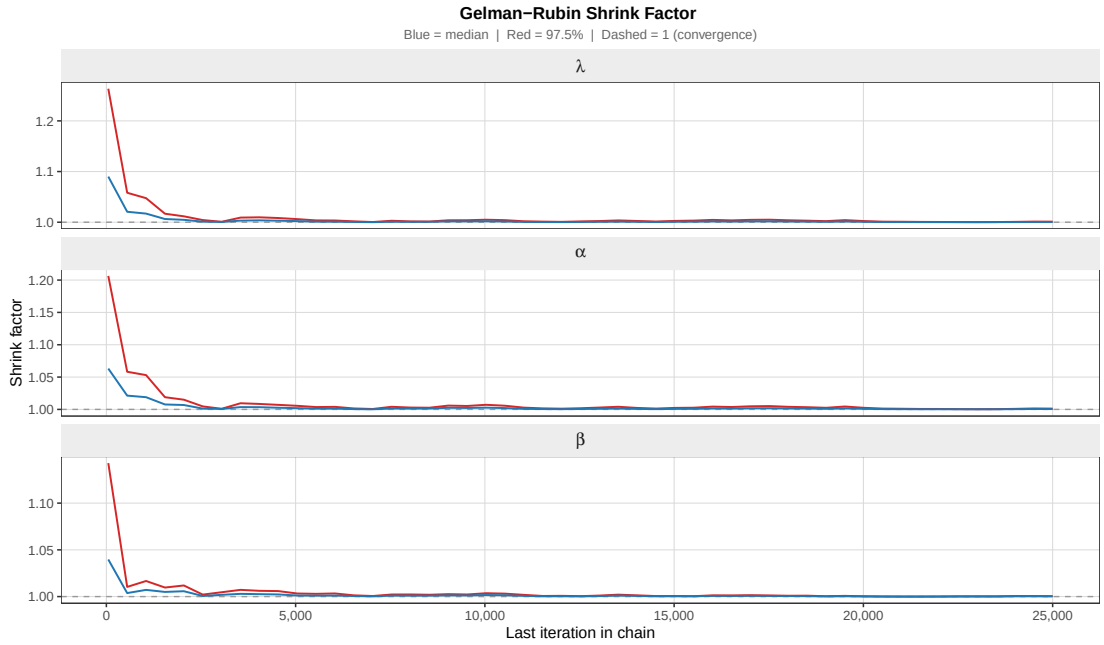


Figure 13. Gelman–Rubin shrink factor plots for the parameters λ, α, and β under Prior 1 based on Set I.

6. Real data analysis

This section analyzes two real datasets to illustrate the practical applicability of the GHj model: The aircraft windshield service time data and blood cancer patients' lifetime data. Classical and Bayesian inference is considered, and the GHj model is compared with its Hj, Weibull, and Lomax submodels, as well as the WL and FWE models as competitive models with CDFs given, respectively, by

$$F_{\mathrm{WL}}(x;a,b,\alpha,\beta) = 1-\exp\left\{-a\left[\left(1+\frac{x}{\beta}\right)^{\alpha}-1\right]^{b}\right\}, \qquad x>0$$

and

$$F_{\mathrm{FWE}}(x;\alpha,\beta) = 1-\exp\left\{-\exp\left(\alpha x-\frac{\beta}{x}\right)\right\}, \qquad x>0,$$

where $a,b,\alpha,\beta>0$.

The model's performance is assessed using the Akaike information criterion (AIC), Bayesian information criterion (BIC), consistent Akaike information criterion (CAIC), and Hannan–Quinn information criterion (HQIC), together with the Kolmogorov–Smirnov (KS), Anderson–Darling (AD), and Cramér–von Mises (CvM) goodness-of-fit statistics and their parametric-bootstrap p-values. The CAIC, using Bozdogan's definition, and the HQIC are calculated as

$$\mathrm{CAIC} = -2l + k(\log n + 1), \qquad \mathrm{HQIC} = -2l + 2k\log(\log n),$$

where l denotes the fitted maximized log-likelihood, k is the number of estimated parameters, and n is the sample size. Graphical assessment is additionally based on fitted densities, probability–probability (PP) plots, quantile–quantile (QQ) plots, and empirical and fitted RFs.

6.1. Application I

The first dataset consists of the service times of 63 aircraft windshields, originally reported by Murthy et al. [30] and later analyzed by Tahir et al. [23]. Analyzing such service times is essential for improving maintenance planning, thereby enhancing aircraft reliability and operational safety. The observed failure times are presented in Table 2.

Table 2. Service times of aircraft windshield.

0.046	1.436	2.592	0.140	1.492	2.600	0.150	1.580	2.670	0.248
1.719	2.717	0.280	1.794	2.819	0.313	1.915	2.820	0.389	1.920
2.878	0.487	1.963	2.950	0.622	1.978	3.003	0.900	2.053	3.102
0.952	2.065	3.304	0.996	2.117	3.483	1.003	2.137	3.500	1.010
2.141	3.622	1.085	2.163	3.665	1.092	2.183	3.695	1.152	2.240
4.015	1.183	2.341	4.628	1.244	2.435	4.806	1.249	2.464	4.881
1.262	2.543	5.140							

Tables 3 and 4 compare the GHj model with the Hj, Weibull, Lomax, WL, and FWE models. Table 3 reports the likelihood estimates together with their parametric-bootstrap SEs, whereas Table 4 presents the AIC, BIC, CAIC, and HQIC, along with the KS, AD, and CvM goodness-of-fit statistics. The corresponding p-values were obtained from 400 parametric-bootstrap replications, with all unknown parameters re-estimated in each bootstrap sample. The GHj model yields the largest fitted log-likelihood, whereas the Hj model has the smallest AIC, BIC, CAIC, and HQIC values. In terms of goodness of fit, the GHj model produces the smallest KS, AD, and CvM statistics, with corresponding bootstrap p-values well above the 5% significance level, indicating the closest empirical agreement among the models considered under all three goodness-of-fit measures. The Hj, Weibull, and WL models also provide adequate fits according to these tests, whereas the Lomax and FWE models are rejected by all three goodness-of-fit tests.

Table 3. Likelihood estimates with bootstrap SEs for the aircraft windshield data.

Quantity	GHj	Hj	Weibull	Lomax	WL	FWE
Parameter order	(λ,α,β)	(λ,α)	(λ,β)	α	(a,b,α,β)	(α,β)
First parameter	0.080649 (0.059320)	0.280606 (0.050687)	0.255693 (0.056795)	0.962509 (0.122127)	0.123329 (0.089017)	0.294379 (0.038691)
Second parameter	0.238782 (0.129771)	0.169224 (0.093502)	1.629045 (0.156948)	–	0.916108 (0.693641)	0.663924 (0.101814)
Third parameter	2.399255 (0.576798)	–	–	–	3.864444 (1.678245)	–
Fourth parameter	–	–	–	–	2.884565 (1.281905)	–

*Note: Dashes indicate parameters that have not been estimated.

Table 4. Information criteria and goodness-of-fit results for the aircraft windshield data.

Model	Log-likelihood	AIC	BIC	CAIC	HQIC	KS	KS p-value	AD	AD p-value	CvM	CvM p-value
GHj	−97.90636	201.8127	208.2421	211.2421	204.3414	**0.059384**	0.6384	**0.210424**	0.6633	**0.029960**	0.6409
Hj	−98.42015	**200.8403**	**205.1266**	**207.1266**	**202.5261**	0.088511	0.3117	0.302336	0.6234	0.051898	0.5362
Weibull	−100.31770	204.6354	208.9217	210.9217	206.3212	0.108686	0.0723	0.642591	0.1072	0.092938	0.1421
Lomax	−130.86129	263.7226	265.8657	266.8657	264.5655	0.318008	0.0025	9.139875	0.0025	1.857122	0.0025
WL	−98.11700	204.2340	212.8065	216.8065	207.6056	0.066089	0.5436	0.236532	0.5985	0.034065	0.5935
FWE	−119.35247	242.7049	246.9912	248.9912	244.3907	0.323861	0.0025	10.549712	0.0025	2.305313	0.0025

For additional graphical validation, Figure 14 presents the histogram with the fitted density, PP plot,

QQ plot, and empirical and fitted RFs. The fitted density follows the observed data closely, while the PP and QQ plots show good agreement between the empirical and fitted distributions. The empirical and fitted RFs also exhibit close agreement over the observed range.

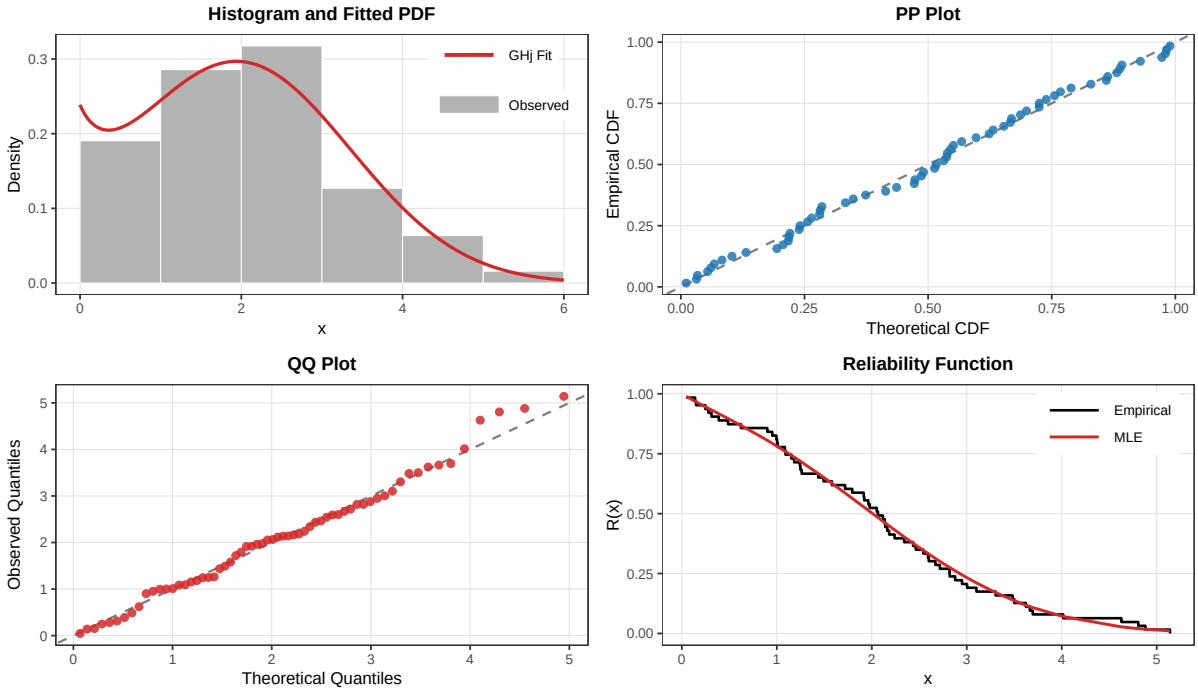


Figure 14. Graphical assessment of the GHj model's fit for the aircraft windshield data.

Formal comparisons of the GHj model with the Hj, Weibull, and Lomax submodels were performed using parametric bootstrap likelihood-ratio tests (LRTs). The corresponding restrictions are $\beta = 2$, $\alpha = 0$, and $\lambda = 0$, respectively. Both the GHj and restricted models were refitted in each of 400 bootstrap replications. The results are reported in Table 5. The bootstrap LRT provides insufficient evidence against the Hj restriction, whereas the Weibull and Lomax restrictions are rejected at the 5% significance level. Hence, the results support the additional flexibility of the GHj model relative to the Weibull and Lomax submodels, while the Hj specification remains adequate for this particular dataset.

Table 5. Parametric bootstrap LRTs for the GHj submodels.

Null model	Null restriction	LRT statistic	Bootstrap p-value	Successful replications
Hj	$\beta = 2$	1.0276	0.3217	400/400
Weibull	$\alpha = 0$	4.8227	0.0150	400/400
Lomax	$\lambda = 0$	65.9099	0.0025	400/400

Figure 15 presents the profile log-likelihood curves for the three GHj parameters. Each profile exhibits a single peak over the examined range near the corresponding fitted value, supporting the numerical behavior of the fitted solution.

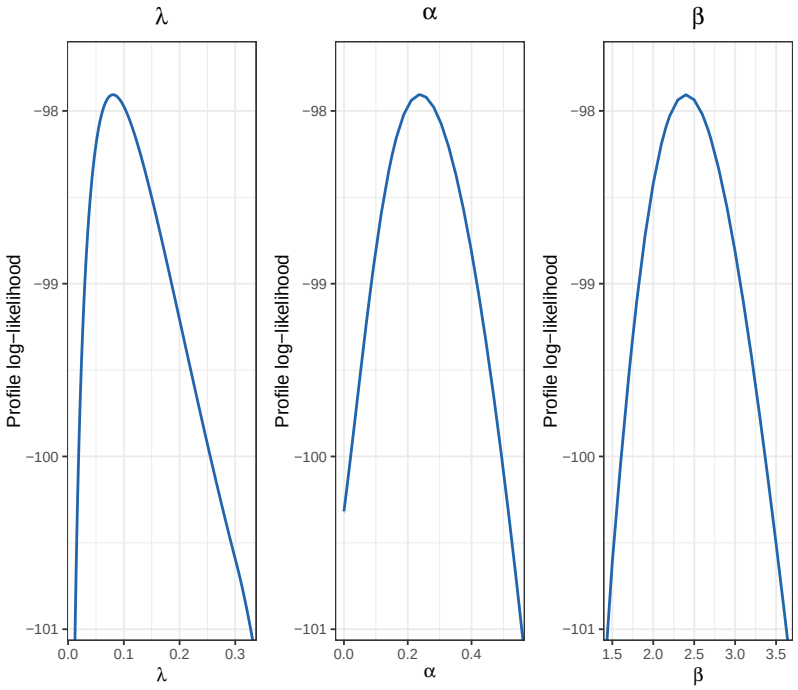


Figure 15. Profile log-likelihood curves for the GHj parameters based on the aircraft windshield data.

The observed information matrix at the fitted GHj solution is positive definite, with eigenvalues 6247.2927, 125.0593, and 5.7373, and a condition number of approximately 1088.90. The correlation matrix of the parameter estimators is presented in Table 6. The strongest association occurs between λ and β, with a correlation of -0.9574.

Table 6. Correlation matrix of the GHj parameter estimators derived from the observed information.

	λ	α	β
λ	1.0000	−0.6396	−0.9574
α	−0.6396	1.0000	0.5685
β	−0.9574	0.5685	1.0000

To provide interval estimates that do not rely on the observed information matrix, 95% parametric bootstrap percentile intervals were obtained from 400 replications and are reported in Table 7.

Table 7. Likelihood estimates, bootstrap SEs, and 95% bootstrap percentile intervals for GHj model.

Parameter	Estimate	Lower limit	Upper limit
λ	0.080649	0.011182	0.232745
α	0.238782	0.073026	0.504304
β	2.399255	1.735232	3.882940

For the Bayesian analysis, independent gamma$(1, 0.001)$ priors were assigned to the three parameters. Table 8 reports the Bayes estimates under squared error loss, posterior standard deviations (SDs), 95% equal-tail credible intervals, effective sample sizes (ESSs), Monte Carlo standard errors (MCSEs), and Geweke statistics.

Table 8. Bayesian estimates, posterior uncertainty, and simulation diagnostics for the GHj model.

Parameter	Bayes estimate (posterior SD)	95% credible interval	ESS	MCSE	Geweke statistic
λ	0.110563 (0.059310)	(0.029437, 0.257246)	3132.6	0.001060	−0.58022
α	0.236652 (0.109539)	(0.045036, 0.473075)	3364.6	0.001888	0.01202
β	2.268821 (0.380596)	(1.585312, 3.072110)	2928.2	0.007033	0.43889

The ESS measures the effective number of approximately independent posterior draws, whereas the MCSE quantifies the simulation error in the estimated posterior means. The ESS values are sufficiently large and the MCSEs are small relative to the corresponding posterior SDs. The Geweke diagnostic compares the means of early and late portions of the Markov chain, with values close to zero indicating no evidence of a systematic difference between these portions. Here, all Geweke statistics lie well within $(-1.96, 1.96)$. Together, these diagnostics indicate the adequate numerical performance of the posterior simulation.

Figures 16 and 17 illustrate the marginal posterior distributions of the GHj parameters based on the retained MCMC samples. The posterior densities are smooth and unimodal, with mild right skewness for λ and α, while the posterior distribution of β is more symmetric and concentrated around its center. The violin plots provide a complementary representation of the posterior location and spread and are consistent with the density plots and the posterior summaries reported in Table 8.

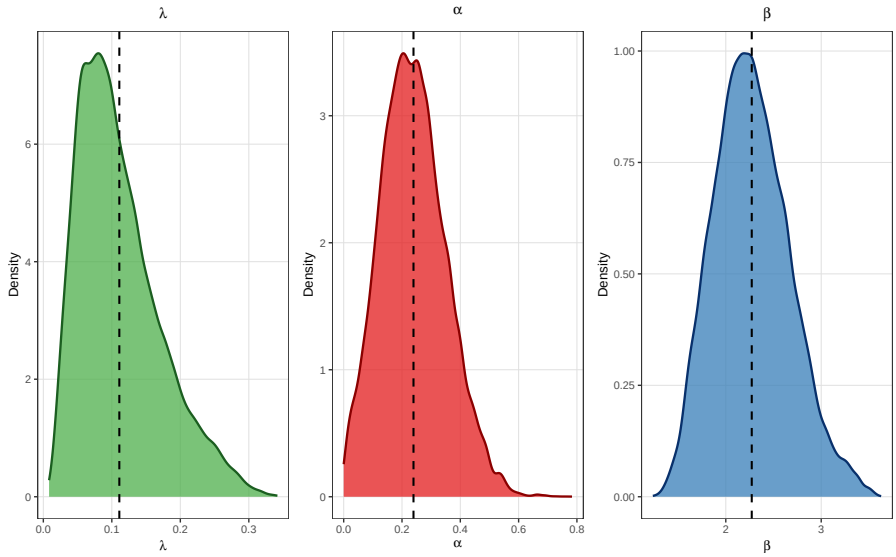


Figure 16. Posterior density estimates of λ, α, and β for the aircraft windshield data. The dashed vertical lines indicate the corresponding posterior means.

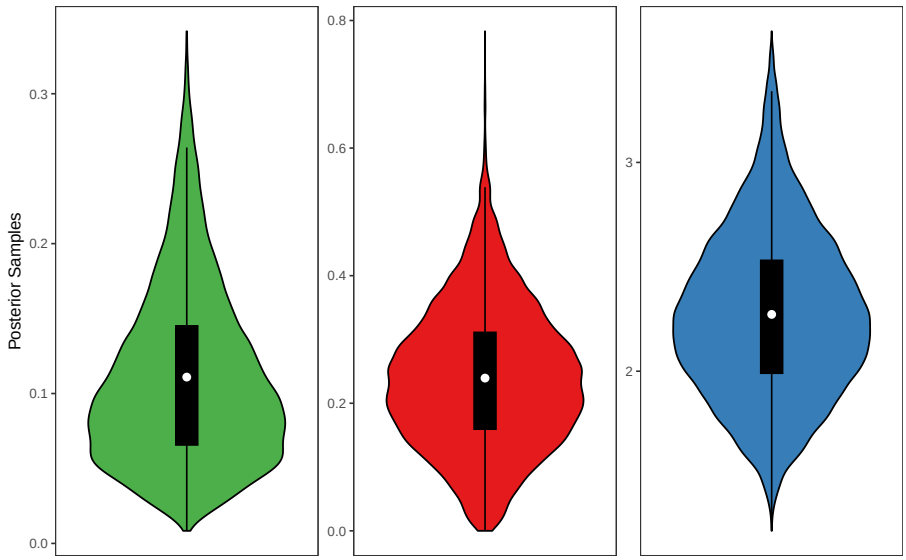


Figure 17. Violin plots of λ (left), α (middle), and β (right) for the aircraft windshield data. The white dots represent the posterior means.

6.2. Application II

The second application considers the lifetimes, measured in years, of 40 patients with blood cancer treated at a hospital affiliated with the Ministry of Health in Saudi Arabia. The specific type of blood cancer was not reported. These data were studied by Abouammoh et al. [31] and were recently analyzed by Alhidairah et al. [32]. The observations are presented in Table 9.

Table 9. Lifetimes (years) of 40 patients with blood cancer.

0.315	0.496	0.698	1.144	1.207	1.262	1.413	2.023	2.034	2.160
2.209	2.368	2.530	2.691	2.804	2.908	2.910	3.190	3.233	3.346
3.346	3.425	3.496	3.532	3.715	3.748	3.855	3.984	4.047	4.241
4.320	4.320	4.378	4.389	4.394	4.643	4.750	4.925	4.969	5.070

For the patients' lifetime data, the parameter estimates and their parametric bootstrap SEs are summarized in Table 10, while the comparative fit results are presented in Table 11. The latter includes the maximized log-likelihood, four information criteria, and the KS, AD, and CvM statistics with their bootstrap p-values. The bootstrap calculations are based on 400 replications, with models' parameters re-estimated for each generated sample. Among the six fitted distributions, GHj achieves the lowest values of AIC, BIC, CAIC, and HQIC. The WL model gives a slightly higher maximized log-likelihood, but this improvement is offset by its additional parameter, leading to larger values of all four information criteria. The empirical distribution of the data is also closely represented by GHj, which records the smallest KS, AD, and CvM statistics, with none of the corresponding bootstrap tests indicating a lack of fit at the 5% level. The WL model likewise provides an acceptable fit. In contrast, the Hj, Lomax, and FWE models are rejected by all three goodness-of-fit tests, while the Weibull model is rejected according to the AD and CvM tests. Taken together, these results favor the GHj specification

for the patient lifetime data.

It is important to note that the WL fit requires some caution in this application. Examination of the likelihood from multiple starting values showed that its last two parameter estimates increase substantially while their ratio remains nearly constant and the log-likelihood approaches a stable limiting value. This behavior indicates a nearly flat likelihood direction and poor practical identification of these two parameters, a phenomenon associated with flat or nearly flat likelihood surfaces, as discussed by Rubio et al. [33]. Consequently, their individual estimates and bootstrap SEs are not reported. Nevertheless, the fitted log-likelihood and goodness-of-fit measures remain essentially unchanged along this limiting direction, and the WL model is therefore retained for comparative purposes.

Table 10. Likelihood estimates with bootstrap SEs for the patient lifetime data.

Quantity	GHj	Hj	Weibull	Lomax	WL	FWE
Parameter order	(λ, α, β)	(λ, α)	(λ, β)	α	(a, b, α, β)	(α, β)
First parameter	0.001627 (0.003599)	0.175736 (0.029358)	0.040073 (0.019095)	0.741239 (0.120701)	0.041562 (0.014705)	0.310383 (0.042132)
Second parameter	0.168690 (0.073999)	0 (–)	2.577038 (0.333641)	–	0.849064 (0.363537)	2.986975 (0.520041)
Third parameter	4.649960 (1.010177)	–	–	–	–	–
Fourth parameter	–	–	–	–	–	–

*Note: For Hj, $\widehat{\alpha} = 0$, so the fitted model reduces to the Rayleigh distribution. Dashes indicate parameters that have not been estimated. For the WL model, the last two parameter estimates are not reported because the likelihood approaches a limiting region as both parameters increase while their ratio remains approximately constant.

Table 11. Information criteria and goodness-of-fit results for the patients' lifetime data.

Model	Log-likelihood	AIC	BIC	CAIC	HQIC	KS	KS p-value	AD	AD p-value	CvM	CvM p-value
GHj	−64.64646	**135.2929**	**140.3596**	**143.3596**	**137.1249**	**0.078207**	0.5611	**0.243975**	0.5486	**0.028370**	0.7032
Hj	−69.96306	143.9261	147.3039	149.3039	145.1474	0.166048	0.0299	1.495795	0.0100	0.289192	0.0050
Weibull	−68.38538	140.7708	144.1485	146.1485	141.9921	0.124056	0.1122	0.980967	0.0100	0.135903	0.0175
Lomax	−105.94101	213.8820	215.5709	216.5709	214.4927	0.384566	0.0025	9.515741	0.0025	1.952481	0.0025
WL	**−64.09700**	136.1940	142.9495	146.9495	138.6366	0.078524	0.6683	0.248325	0.6434	0.031623	0.7456
FWE	−74.13915	152.2783	155.6561	157.6561	153.4996	0.226890	0.0025	3.208946	0.0025	0.626753	0.0025

Figure 18 provides a graphical assessment of the fitted GHj model. The histogram and fitted density show close agreement between the observed data and the fitted distribution. The PP and QQ plots similarly show good agreement between the empirical and theoretical probabilities and quantiles, while the empirical and fitted RFs closely follow each other over the observed range.

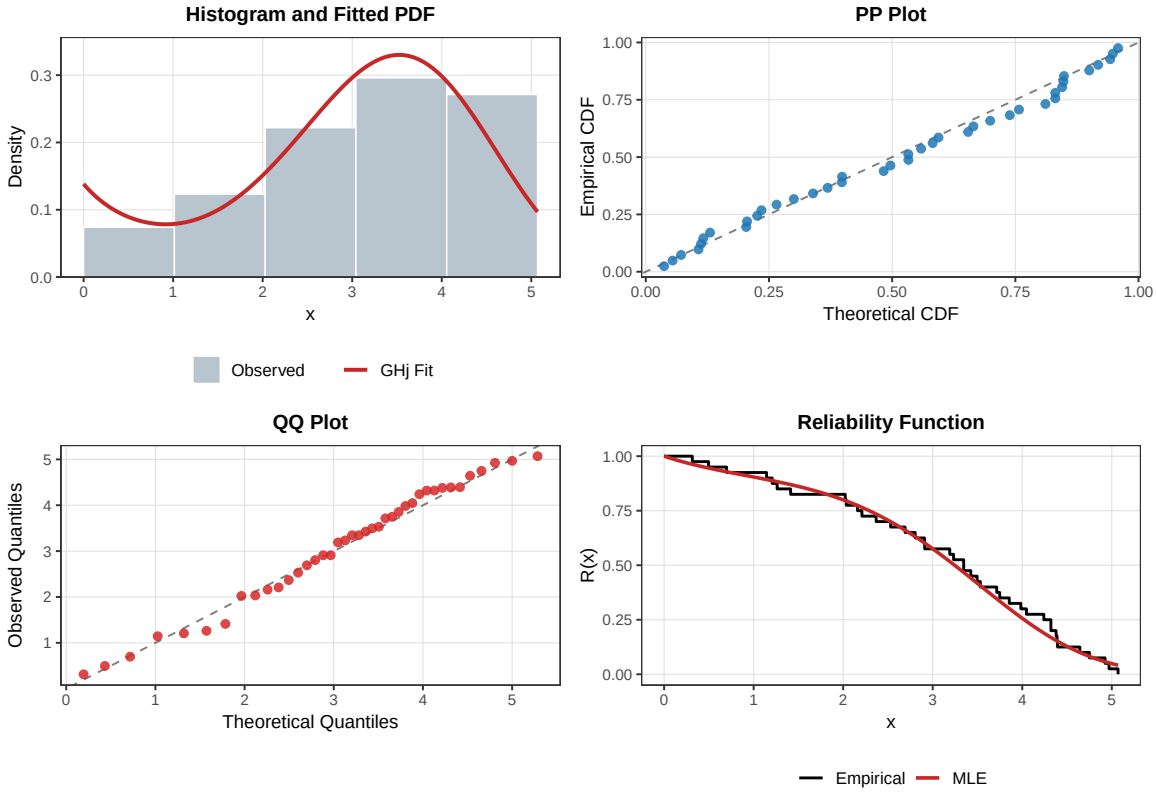


Figure 18. Graphical assessment of the GHj model fit for the patient lifetime data.

Formal comparisons of the GHj model with the Hj, Weibull, and Lomax submodels were performed using parametric bootstrap LRTs. Both the GHj and restricted models were refitted in each of 400 bootstrap replications. The results are reported in Table 12. All three bootstrap p-values are below 0.05, providing evidence against the corresponding Hj, Weibull, and Lomax restrictions and supporting the additional flexibility of the GHj model for these data.

Table 12. Parametric-bootstrap LRTs for the GHj submodels.

Null model	Null restriction	LRT statistic	Bootstrap p-value	Successful replications
Hj	$\beta = 2$	10.6332	0.0025	400/400
Weibull	$\alpha = 0$	7.4778	0.0075	400/400
Lomax	$\lambda = 0$	82.5891	0.0025	400/400

Figure 19 presents the profile log-likelihood curves for the three GHj parameters. Each profile exhibits a single peak over the examined range near the corresponding fitted value, supporting the numerical behavior of the fitted solution.

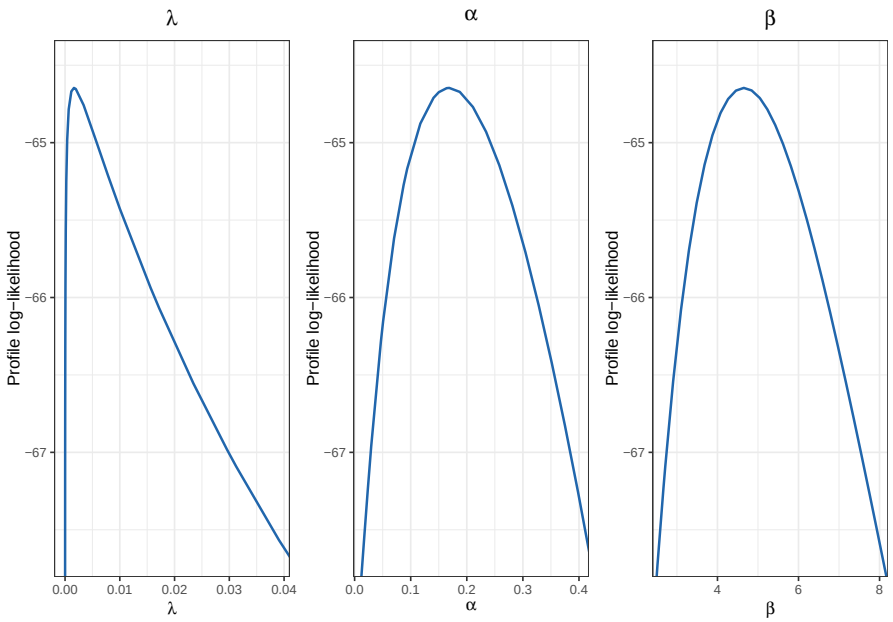


Figure 19. Profile log-likelihood curves for the GHj parameters based on the patient lifetime data.

The observed information matrix at the fitted GHj solution is positive definite, with the eigenvalues 1.055968×10^7, 205.8965, and 0.8956141, and a condition number of approximately 1.179043×10^7. The correlation matrix of the parameter estimators is presented in Table 13. The strongest association is between λ and β, with a correlation of -0.9928. The observed information diagnostics indicate substantial dependence between λ and β for this dataset, as reflected by the large condition number and their strong negative correlation. The bootstrap variability of $\hat{\lambda}$ also indicates that λ is estimated with relatively low precision. These findings suggest that the individual parameter estimates, particularly λ and β, should be interpreted cautiously, even though the observed information matrix is positive definite at the fitted solution.

Table 13. Correlation matrix of the GHj parameter estimators derived from the observed information.

	λ	α	β
λ	1.000000	−0.529901	−0.992801
α	−0.529901	1.000000	0.510475
β	−0.992801	0.510475	1.000000

To provide interval estimates that do not rely on the observed information matrix, 95% parametric-bootstrap percentile intervals were obtained from 400 replications. The results are presented in Table 14.

The bootstrap intervals in Table 14 quantify the uncertainty associated with the parameter estimates. More importantly, the bootstrap LRT results provide direct evidence against the nested Hj, Weibull, and Lomax restrictions, while the profile log-likelihoods and goodness-of-fit measures provide complementary information on the fitted GHj model.

Table 14. Likelihood estimates and 95% bootstrap percentile intervals for GHj model.

Parameter	Estimate	Lower limit	Upper limit
λ	0.001627	0.00003566	0.01393883
α	0.168690	0.03750026	0.32270091
β	4.649960	3.328699	7.146697

For the Bayesian analysis, independent gamma$(1, 0.001)$ priors were assigned to the three parameters. Table 15 reports the Bayes estimates under squared error loss, posterior SDs, 95% equal-tail credible intervals, and posterior simulation diagnostics.

Table 15. Bayesian estimates, posterior uncertainty, and simulation diagnostics for the GHj model.

Parameter	Bayes estimate (posterior SD)	95% credible interval	ESS	MCSE	Geweke statistic
λ	0.011806 (0.013365)	(0.000506, 0.049516)	2503.9	0.000267	0.37662
α	0.149774 (0.076041)	(0.027326, 0.321013)	3044.1	0.001378	0.88428
β	3.725204 (0.772986)	(2.410240, 5.411680)	2249.6	0.016297	−0.04545

The ESS and MCSE values indicate adequate numerical precision of the posterior estimates, while all Geweke statistics lie within $(-1.96, 1.96)$. Figures 20 and 21 illustrate the corresponding posterior distributions. The posterior densities are unimodal, with λ showing noticeable right skewness, while the distributions of α and β are more concentrated around their posterior means. The posterior distribution of λ is noticeably right-skewed, which also contributes to the difference between its posterior mean and the MLE. The violin plots provide a complementary representation of the posterior spread and location, and are consistent with the density plots and the posterior summaries reported in Table 15.

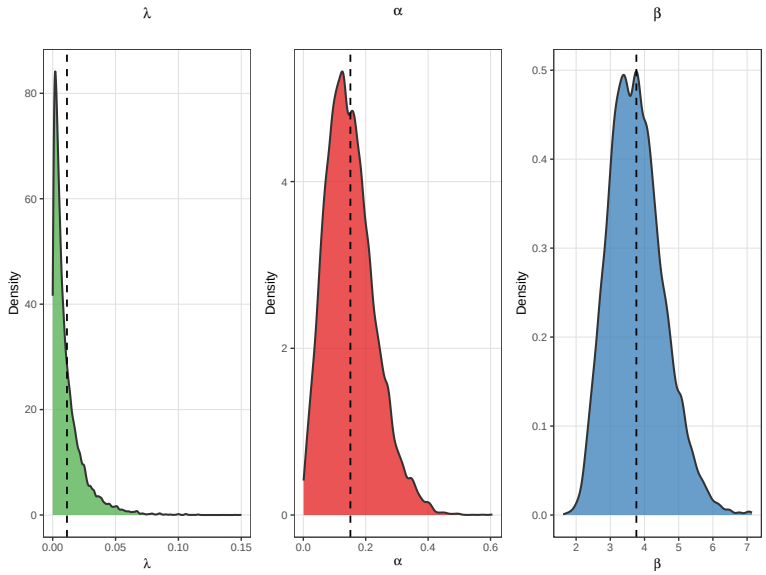


Figure 20. Posterior density estimates of λ, α, and β for the patient lifetime data. The dashed vertical lines indicate the corresponding posterior means.

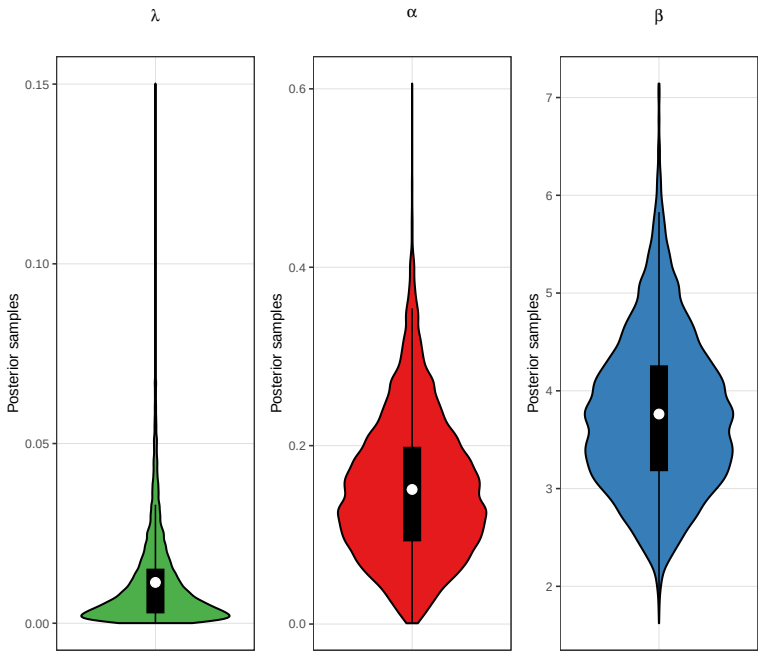


Figure 21. Violin plots of λ (left), α (middle), and β (right) for the patients' lifetime data. The white dots represent the posterior means.

Overall, the two applications demonstrate the practical flexibility of the GHj model under different data characteristics. For the aircraft windshield data, GHj model provides the smallest KS, AD, and CvM statistics, although the information criteria favor the simpler Hj submodel and the bootstrap LRT does not reject the Hj restriction. In contrast, for the patients' lifetime data, the GHj model yields the smallest information criteria and goodness-of-fit statistics, while the bootstrap LRTs reject the Hj, Weibull, and Lomax restrictions. Taken together, these results show that the GHj provides a consistently strong fit across both datasets, while the extent to which its additional flexibility is required depends on the characteristics of the data.

7. Conclusions

In this study, a new and flexible lifetime model, referred to as the generalized Hjorth model, has been proposed to provide an effective framework for modeling complex reliability data. Graphical illustrations demonstrate that the model can exhibit different probability density function shapes under selected parameter configurations, while its hazard rate function accommodates diverse behaviors, including decreasing, increasing, bathtub-shaped, and increase–decrease–increase patterns. A theoretical investigation of the proposed model has been presented. Several important statistical characteristics have been investigated, including its moments, order statistics, Rényi entropy, and stress–strength reliability, while random variate generation has been implemented using the competing-risks representation. Parameter estimation has been carried out using both maximum likelihood and Bayesian approaches. Owing to the nonlinear nature of the likelihood equations, numerical optimization techniques have been used to obtain the maximum likelihood estimates, while Bayesian inference has been implemented via Markov chain Monte Carlo methods under the squared error

loss function. The performance of the estimators has been examined through simulation studies, with the results showing generally improved estimation accuracy as the sample size increases under the parameter settings considered. The practical applicability of the generalized Hjorth model has been illustrated through the analysis of two real datasets. The results show that the proposed model provides a good fit to both datasets, as supported by the goodness-of-fit measures and graphical assessments. Comparative analyses with the considered competing models further indicate that the proposed model can provide useful additional flexibility, although its relative performance depends on the characteristics of the data. Overall, the findings suggest that the generalized Hjorth model represents a useful addition to the class of lifetime distributions, offering flexible modeling capability and practical statistical inference. The model may be applied in various fields such as reliability engineering, survival analysis, and applied statistics.

Several limitations should be acknowledged. The simulation study considers only two parameter configurations and does not cover all hazard rate function shapes supported by the generalized Hjorth distribution; thus, the reported finite-sample results are specific to the settings examined, and the advantage of Prior 1 should be interpreted in light of its centering at the true parameter values. Estimates near parameter boundaries and strong correlations among parameter estimates may also affect the precision of the estimations, while Bayesian results may be sensitive to the prior specification, particularly for small samples. Moreover, the real-data comparisons are limited to the two datasets considered and do not establish general superiority over competing distributions. The present three-parameter formulation also inherits the unit-scale structure of the Hjorth model and is therefore not invariant to changes in the measurement unit; introducing an explicit scale parameter represents a useful direction for future extension. Finally, the present analysis is restricted to complete samples, and extending the proposed inference procedures to censored data, broader parameter configurations, alternative priors, and additional applications represents an important direction for future research.

Use of Generative-AI tools declaration

The author declares that he has not used Artificial Intelligence (AI) tools in the creation of this article.

Funding

The author gratefully acknowledge the Deanship of Scientific Research (DSR) at King Abdulaziz University, Jeddah, Saudi Arabia, for funding this project under grant No. (IPP: 182-130-2026) and for providing technical support.

Conflicts of interest

The author declares no conflict of interest.

References

1. A. Azzalini, A class of distributions which includes the normal ones, *Scand. J. Stat.*, 1985, 171–178.

2. G. S. Mudholkar, D. K. Srivastava, Exponentiated Weibull family for analyzing bathtub failure-rate data, *IEEE T. Reliab.*, **42** (1993), 299–302. https://doi.org/10.1109/24.229504
3. A. W. Marshall, I. Olkin, A new method for adding a parameter to a family of distributions with application to the exponential and Weibull families, *Biometrika*, **84** (1997), 641-652. https://doi.org/10.1093/biomet/84.3.641
4. A. Mahdavi, D. Kundu, A new method for generating distributions with an application to exponential distribution, *Commun. Stat.-Theor. M.*, **46** (2017), 6543–6557. https://doi.org/10.1080/03610926.2015.1130839
5. N. Eugene, C. Lee, F. Famoye, Beta-normal distribution and its applications, *Commun. Stat.-Theor. M.*, **31** (2002), 497–512. https://doi.org/10.1081/STA-120003130
6. A. Alzaatreh, C. Lee, F. Famoye, A new method for generating families of continuous distributions, *Metron*, **71** (2013), 63–79. https://doi.org/10.1007/s40300-013-0007-y
7. C. Lee, F. Famoye, A. Y. Alzaatreh, Methods for generating families of univariate continuous distributions in the recent decades, *WIRES Comput. Stat.*, **5** (2013), 219–238. https://doi.org/10.1002/wics.1255
8. M. C. Jones, On families of distributions with shape parameters, *Int. Stat. Rev.*, **83** (2015), 175–192. https://doi.org/10.1111/insr.12055
9. M. A. Abdelaziz, G. M. Cordeiro, Z. M. Nofal, A. Z. Afify, A Comprehensive Survey of Weibull-Based Families, *J. Stat. Model. Meth.*, **1** (2025), 98–118. https://doi.org/10.65905/zr8pgy41
10. U. Hjorth, A reliability distribution with increasing, decreasing, constant and bathtub-shaped failure rates, *Technometrics*, **22** (1980), 99–107.
11. F. Guess, K. H. Nam, Failure rate and mean residual life with trend changes, *Asia Pac. J. Oper. Res.*, **15** (1998).
12. A. S. Yadav, H. S. Bakouch, C. Chesneau, Bayesian estimation of the survival characteristics for Hjorth distribution under progressive type-II censoring, *Commun. Stat.-Simul. C.*, **51** (2020), 882–900. https://doi.org/10.1080/03610918.2019.1659363
13. N. Pushkarna, J. Saran, K. Verma, Progressively Type-II right censored order statistics from Hjorth distribution and related inference, Statistics, *Optim. Inform. Comput.*, **8** (2020), 481–498. https://doi.org/10.19139/soic-2310-5070-751
14. A. Elshahhat, M. Nassar, Bayesian survival analysis for adaptive Type-II progressive hybrid censored Hjorth data, *Computation. Stat.*, **36** (2021), 1965–1990. https://doi.org/10.1007/s00180-021-01065-8
15. R. Alotaibi, M. Nassar, A. Elshahhat, Analysis of unified hybrid Hjorth competing risk data and its application to multiple myeloma and electrical appliances, *J. Math.*, **2025** (2025), 5089157. https://doi.org/10.1155/jom/5089157
16. M. Xie, C. D. Lai, Reliability analysis using an additive Weibull model with bathtub-shaped failure rate function, *Reliab. Eng. Syst. Safe.*, **52** (1996), 87–93. https://doi.org/10.1016/0951-8320(95)00149-2
17. F. K. Wang, A new model with bathtub-shaped failure rate using an additive Burr XII distribution, *Reliab. Eng. Syst. Safe.*, **70** (2000), 305–312. https://doi.org/10.1016/S0951-8320(00)00066-1

18. B. Singh, An additive Perks–Weibull model with Bathtub-shaped hazard rate function, *Commun. Math. Stat.*, **4** (2016), 473–493. https://doi.org/10.1007/s40304-016-0096-z
19. L. C. Méndez-González, L. A. Rodríguez-Picón, I. J. C. Pérez-Olguín, L. R. Vidal Portilla, An additive Chen distribution with applications to lifetime data, *Axioms*, *12* (2023), 118. https://doi.org/10.3390/axioms12020118
20. M. G. M. Ghazal, Hamiltonian Monte Carlo–based inference for the flexible exponential power–Weibull distribution with applications in reliability analysis, *AIMS Math.*, **11** (2026), 11659–11705. https://doi.org/10.3934/math.2026481
21. A. J. Jr Hallinan , A review of the Weibull distribution, *J. Qual. Technol.*, **25** (1993), 85–93. https://doi.org/10.1080/00224065.1993.11979431
22. H. Pham, C. D. Lai, On recent generalizations of the Weibull distribution, *IEEE T. Reliab.*, **56** (2007), 454–458. https://doi.org/10.1109/TR.2007.903352
23. M. H. Tahir, G. M. Cordeiro, M. Mansoor, M. Zubair, The Weibull-Lomax distribution: Properties and applications, *Hacet. J. Math. Stat.*, **44** (2015), 455–474.
24. M. Bebbington, C. D. Lai, R. Zitikis, A flexible Weibull extension, *Reliab. Eng. Syst. Safe.*, **92** (2007), 719–726. https://doi.org/10.1016/j.ress.2006.03.004
25. T. Liu, R. Xue, A convergent multi-step efficient iteration method to solve nonlinear equation systems, *J. Appl. Math. Comput.*, **71** (2025), 2571–2588. https://doi.org/10.1007/s12190-024-02324-9
26. N. Bouguila, D. Ziou, E. Monga, Practical Bayesian estimation of a finite beta mixture through Gibbs sampling and its applications, *Stat. Comput.*, **16** (2006), 215–225. https://doi.org/10.1007/s11222-006-8451-7
27. M. J. Zyphur, F. L. Oswald, Bayesian estimation and inference: A user's guide, *J. Manage.*, **41** (2015), 390–420.
28. N. Metropolis, A. W. Rosenbluth, M. N. Rosenbluth, A. H. Teller, E. Teller, Equation of state calculations by fast computing machines, *J. Chem. Phys.*, **21** (1953), 1087–1092.
29. W. K. Hastings, Monte Carlo sampling methods using Markov chains and their applications, *Biometrika*, **57** (1970), 97–109. https://doi.org/10.1093/biomet/57.1.97
30. D. P. Murthy, M. Xie, R. Jiang, *Weibull models*, John Wiley & Sons, 2004.
31. A. M. Abouammoh, S. A. Abdulghani, I. S. Qamber, On partial orderings and testing of new better than renewal used classes, *Reliab. Eng. Syst. Safe.*, **43** (1994), 37–41. https://doi.org/10.1016/0951-8320(94)90094-9
32. S. Alhidairah, F. M. A. Alam, M. Nassar, A new competing risks model with applications to blood cancer data, *J. Radiat. Res. Appl. Sc.*, **17** (2024), 101001. 10.1016/j.jrras.2024.101001
33. F. J. Rubio, J. A. Espindola, J. A. Montoya, On near-redundancy and identifiability of parametric hazard regression models under censoring, *Biometrical J.*, **65** (2023), 2300006. https://doi.org/10.1002/bimj.202300006

AIMS Press

© 2026 the Author(s), licensee AIMS Press. This is an open access article distributed under the terms of the Creative Commons Attribution License (http://creativecommons.org/licenses/by/4.0)